43rd Aerospace Sciences Meeting & Exhibit
January 10-13, 2005 Reno, NV
AIAA-2005-0075

Characteristics of SLD Ice Accretions on Airfoils and Their Aerodynamic Effects

Andy P. Broeren,[*] Christopher M. LaMarre,[†] Michael B. Bragg,[‡]
University of Illinois at Urbana-Champaign, Urbana, Illinois 61801

and

Sam Lee[§]
QSS Group, Cleveland, OH 44135

Recent aircraft accidents and incidents in Super-cooled, Large Droplet (SLD) conditions has led to the development of a technology roadmap designed to improve the capabilities of SLD engineering tools. Research is required to evaluate and enhance the capabilities of icing test facilities and analytical codes for SLD applications. In support of this effort, the objectives of this study were to identify and document key features of SLD ice accretions on unprotected surfaces and determine their aerodynamic effects. Icing experiments were carried out on a full-scale wing section from a commuter class aircraft. Three key features were determined from the resulting ice accretions: horns, nodules and clear ice. All of the documented ice accretions contained either two or three of these features. Follow-on aerodynamic testing was carried out on a sub-scale model having the same airfoil as the icing model. The ice features were scaled in size by the ratio of the model chord lengths and were simulated with simple geometric materials. Aerodynamic performance measurements were performed at $Re = 1.8\times10^6$ and $Ma = 0.18$ with various combinations of the ice feature simulations applied to the model. The largest performance degradations occurred for SLD accretions having horn features. The relative size of the clear ice region upstream of the horn played an important role in the resulting penalties, while the nodule features downstream of the horn did not. SLD accretion simulations without horns had less of an aerodynamic penalty. The nodule size, spacing and chordwise extent and clear ice thickness and chordwise extent were important factors in the resulting performance.

Nomenclature

α	=	airfoil angle of attack
α_{stall}	=	stalling angle of attack, coincident with $C_{l,max}$
c	=	airfoil chord length
C_d	=	drag coefficient
C_l	=	lift coefficient
$C_{l,max}$	=	maximum lift coefficient
C_m	=	quarter-chord pitching-moment coefficient
k	=	ice roughness height or thickness
Ma	=	freestream Mach number
Re	=	freestream Reynolds number based on chord
x	=	chordwise position along airfoil

[*] Research Scientist, Department of Aerospace Engineering, Senior Member AIAA.
[†] Graduate Research Assistant, Department of Aerospace Engineering, Member AIAA.
[‡] Professor and Head, Department of Aerospace Engineering, Fellow AIAA.
[§] Research Engineer, Member AIAA.

y = normal position from airfoil chord line
LWC = cloud liquid water content
MVD = droplet distribution median volumetric diameter

I. Introduction

It is well known that in-flight icing can result in a loss of lift and increase of drag on an aircraft, resulting in a large performance degradation. Past icing research has been conducted to address the icing conditions described in Appendix C of the Federal Aviation Regulations, Part 25. Recently, research interest has been raised in Supercooled Large Droplet (SLD) icing conditions that are not described in Appendix C. Some of this research has focused on accretions resulting from an active pneumatic ice-protection system. Little research or documentation exists for SLD accretions on unprotected surfaces and the aerodynamic effects remain largely unknown. The purpose of this study was to characterize and document a limited set of SLD accretions, identify the key features of those accretions and identify the aerodynamic significance of the simulated key features.

The 1994 ATR-72 commuter aircraft accident was thought to be caused, in part, by SLD conditions.[1] This accident led to a number of ice accretion and performance studies. For example, Ashenden et al.[2,3] analyzed several University of Wyoming King Air flights in icing. They reported that freezing drizzle exposure resulted in the maximum rate of performance degradation. Wind-tunnel testing performed later showed that more severe aerodynamic penalties were due to the freezing-drizzle case when operation of the deicer was simulated. Icing-tunnel tests were also carried out using wing models with pneumatic deicers. Miller et al.[4] and Addy et al.[5] investigated the effects of temperature, droplet size, airspeed, angle-of-attack, flap setting and deicer cycle time on the resulting ice accretion. A significant result of these tests was the documentation of ice accretion that formed downstream of the ice-protected surfaces. The identification of this spanwise-running ridge ice motivated several aerodynamic studies. For example, Lee and Bragg[6] used a forward-facing quarter-round geometry to simulate the ridge ice. Wind-tunnel tests conducted on NACA 23012 and NLF-0414 airfoil sections indicated that performance effects could be both very severe and highly airfoil dependent.

While these studies have added considerable understanding about SLD accretions and performance effects, they are largely applicable to ice-protected surfaces. SLD ice accretion data on unprotected airfoil surfaces are more scarce. Addy[7] documented a limited set of SLD accretions on a 36-inch chord business jet wing section. These accretions were characterized by the large nodules or feathers well aft of the leading edge typical of SLD accretions. Two primary differences between SLD and Appendix C icing are the increased accretion rates and geometrical feature differences of the SLD accretions. A notable feature of SLD accretions is the nodules or feathers that are found on the aft portion of the accretion.

As described in a paper by Bond et al.,[8] recent aviation accidents and incidents in SLD conditions has forced the possibility that manufacturers may be required to demonstrate safe operation of their aircraft in these conditions. However, current icing test facilities and analytical codes were not developed to model SLD accretions. This has led to the development of a technology roadmap to evaluate and enhance the current icing engineering tools for SLD applications. This study was designed, in part, to support this effort by characterizing SLD ice accretions on unprotected aerodynamic surfaces and evaluating the aerodynamic performance of the key ice accretion features.

This investigation was conducted in two parts. The objective of the first part was to characterize and document a limited set of SLD ice accretions through icing-tunnel testing. Tests were performed on a commuter-class aircraft wing section at the NASA Glenn Research Center Icing Research Tunnel. Key ice features were determined from analysis of the documented accretions. The objective of the second part was to evaluate the aerodynamic penalties of simulated key ice features and SLD ice accretions. The aerodynamic testing was carried out at the University of Illinois on a smaller-scale model having the same airfoil as the icing model. The key ice features were scaled and simulated with geometric shapes to determine the aerodynamic effects.

II. Ice Accretion Testing

A. Experimental Methods

The ice accretion testing was conducted in the NASA Glenn Research Center Icing Research Tunnel, IRT. The IRT is an atmospheric, closed-return wind tunnel capable of maintaining static air temperatures below freezing to -22°F at speeds up to 350 knots. The test section is six feet high and nine feet wide. The model was mounted vertically in the test section and the model angle of attack was controlled by rotating the test-section-floor turntable. The model used in this experiment was a wing section from a commuter class aircraft currently in service. The straight-wing model had a 77.25-inch chord and spanned the six-foot height of the test section. The model was also

equipped with a pneumatic deicer on the leading edge. The deicer covered the leading edge from x/c = 0.11 on the lower surface to x/c = 0.10 on the upper surface. Although the deicer was never activated during these runs, it is important to note since it resulted in a discontinuity on the airfoil surface. Chordwise and spanwise lines were painted on the model to aid in observation. There were three chordwise lines, which were the spanwise location markers. They were located at 31, 36, and 40 inches from the tunnel floor. These three locations correspond to the three stations where the ice accretion tracings were taken. A picture of the model installed in the IRT test section is shown in Fig. 1.

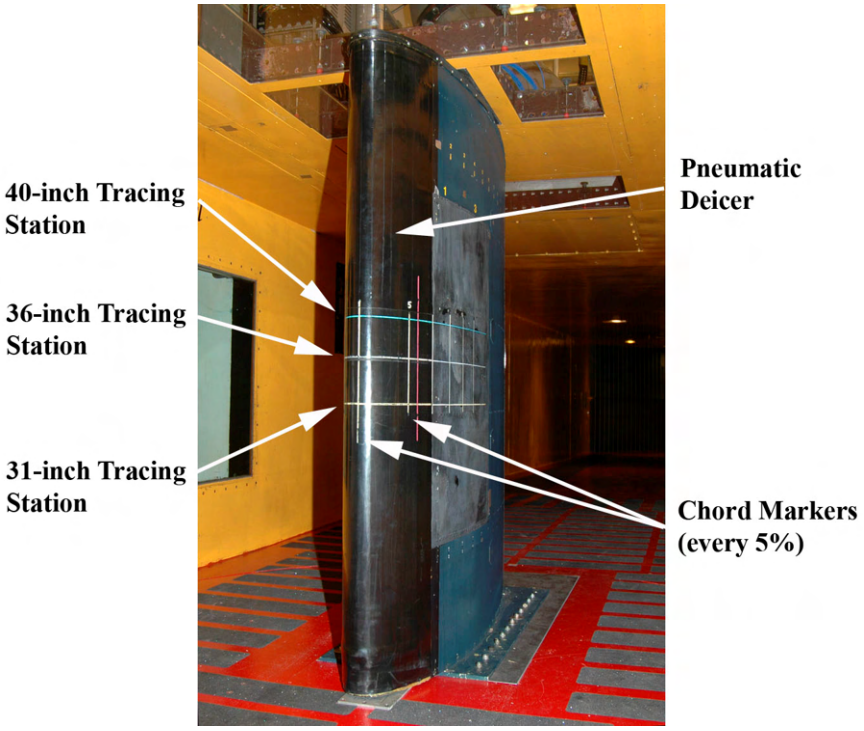

Figure 1. Commuter-class aircraft wing model installed in the IRT test section.

The icing conditions selected for this study were based upon a recent IRT calibration for SLD clouds. All tests were conducted with an icing cloud *MVD* of 133 µm. The corresponding cloud *LWC* was a function of the speed. Airspeeds of 120 and 180 kts were selected as representative of the commuter class wing model. The *LWC* for the two speeds was 0.55 and 0.32 g/m^3, respectively. A total temperature of 28.0 °F with spray times of 10.0 and 22.5 minutes were the most commonly run. The SLD ice accretions documented here resulted from various combinations of these parameters along with variation in angle of attack, either -1 deg. or 3 deg. The nominal Reynolds and Mach numbers for a speed of 120 kts were 8.8×10^6 and 0.18, respectively. The nominal Reynolds and Mach numbers for a speed of 180 kts were 13.3×10^6 and 0.28, respectively.

The limited amount of flight data in actual SLD clouds suggests that the atmospheric *LWC*s are lower than what was available in the IRT for these tests.[9-11] Therefore, an attempt was made to scale the cloud conditions to represent a lower *LWC*. Following the work of Anderson, for geometric scaling, similar methods were applied to the present case.[12] The strategy was to hold the freezing fraction and accumulation parameter constant between the scale and reference cases. Anderson and Tsao[13] noted the importance of the freezing fraction in determining the shape of ice accretions. The freezing fraction was defined by Messinger[14] as the fraction of water flux entering a given control volume that freezes within that control volume. For this study, as with geometric ice-scaling work, the freezing fraction was calculated at the airfoil stagnation point. The accumulation parameter is also non-dimensional and is a measure of the ice mass that accretes over the course of the icing exposure. The values of these parameters and corresponding icing conditions are given in Table 1.

Standard ice accretion documentation was performed after each run. Farfield and close-up photographs were taken from three different views around the leading edge. An “ice-knife” was used to melt the ice accretion at each spanwise station for the tracings. The ice was traced by hand onto a cardboard template. As a result, there was

some uncertainty in the accuracy of the tracings. Also, features such as nodules did not show up as individual features, but as a "height averaged" group. The tracings were later digitized to facilitate plotting and analysis. A digital calipers was used to record ice thickness after the tracings were completed. The maximum thickness measurements were made on the upper and lower surfaces of the airfoil model. These usually corresponded to the horn locations. Thickness measurements were also taken at the estimated stagnation point. Molds were made of the ice accretions from three of the runs. The resulting castings were used for reference and documentation purposes.

B. Results and Discussion

The key features of the SLD accretions were determined from the icing test results. There were three types of features present in the SLD accretions: horns, nodules, and clear ice. It should be noted that there are many different labels that could be applied to a given key feature. For example, nodules and feathers can be difficult to distinguish from one another. This is due to the lack of a universally accepted definition for some of these features. For the purpose of this writing, all features will be referred to as either horns, nodules, or clear ice. Also, the type of ice that composed each feature will be referred to as either rime ice, which freezes upon impact and has a white appearance, or glaze ice, which freezes after impact and has a clear color.

A typical SLD ice accretion generated during this test is shown in Fig. 2 with all three features present. The photographs reveal the clear ice region on the leading edge in the stagnation region of the airfoil. Farther downstream is the distinct horn feature. Less visible in the upper surface view are the nodules. The size and extent of the nodules was much larger on the lower surface of the wing (not shown) since the angle-of-attack was 3 deg. for this case. Each of these features is illustrated in more detail.

The most prominent feature present on many of the accretions was the horns. Figure 3 shows more detailed images of the horn feature from run 593 in Fig. 2. By definition, horns are two dimensional structures. But because of the three dimensional characteristics of the ice from which the horns were formed, they exhibited variations in the surface roughness. The surface location of the horn also had some spanwise variation. This variation could be due, in part, to greater non-uniformity of SLD clouds in the IRT relative to Appendix C conditions.[11] The formation of the horn structures seemed to result from a coalescence of the nodules that formed during the first few minutes of the accretion. For the conditions tested here, this process required several minutes of exposure to the icing cloud. Figure 4 shows an SLD accretion for conditions identical to those of Fig. 2 (and 3), but for a 10-minute exposure. This provides a look at the development of the horn feature. The tracing and photographs in Fig. 4 show that the rows of nodules in the location of the Fig. 2 horn ($x/c \approx 0.01$ to 0.02) have started to form a single structure, but have not grown far enough away from the surface to become a distinct horn feature. A case was also tested where the accretion had both upper and lower surface horn features (see Fig. 5). This was most likely due to the lower angle of attack (-1 deg.) for this case. The formation of the distinct horn features, evident after the 10.6-minute exposure, may have resulted from the lower temperature relative to Figs. 2 and 4. It is noteworthy that distinct horns were only observed at 180 kts and not at 120 kts, with all other conditions constant (except *LWC*). A similar case was run at 150 kts (with intermediate *LWC*) and a horn was also observed in this case. For the 120 kts case, the nodules seemed to coalesce in a streamwise direction, instead of building up in a direction normal to the airfoil surface. More research is required to investigate the important parameters in horn formation. For cases where horns were documented, the heights ranged from a maximum of 2.32 inches ($k/c = 0.0300$) to a minimum of 1.04 inches ($k/c = 0.0135$).

The nodules are the features that are found aft of the horn, or aft of the clear ice in the accretions that lack horns. These are shown in Fig. 6. A nodule refers to an individual, three-dimensional structure. They are almost always found in groups of varying densities and sizes. The individual nodules can be composed of either glaze or rime ice. The surfaces of the glaze ice nodules are generally smooth and the nodules are clear in color. The rime ice nodules have more surface roughness and have a white or opaque appearance. The nodules were common to all of the runs performed, but there were variations in the size, spacing, density and chordwise extent depending upon the aerodynamic and icing conditions. No clear trends were observed, except that the nodules located downstream of large structures tended to be smaller in size. This likely occurred because the larger structures upstream reduced water impingement farther downstream.

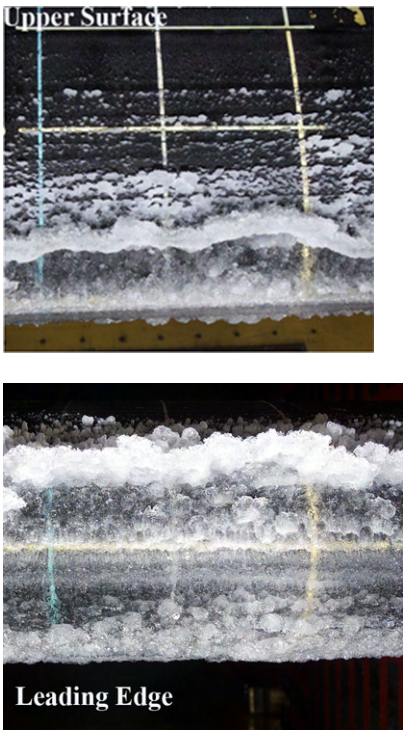

Run	Velocity (kts)	Angle of Attack (deg.)	Total Temp. (°F)	*MVD* (μm)	*LWC* (g/m^3)	Spray Time (min.)
593	180	3	28.0	133	0.32	22.5

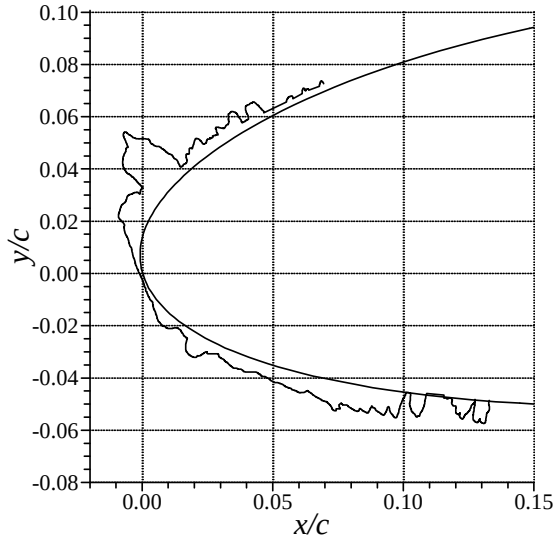

Figure 2. SLD ice accretion exhibiting all three of the key features.

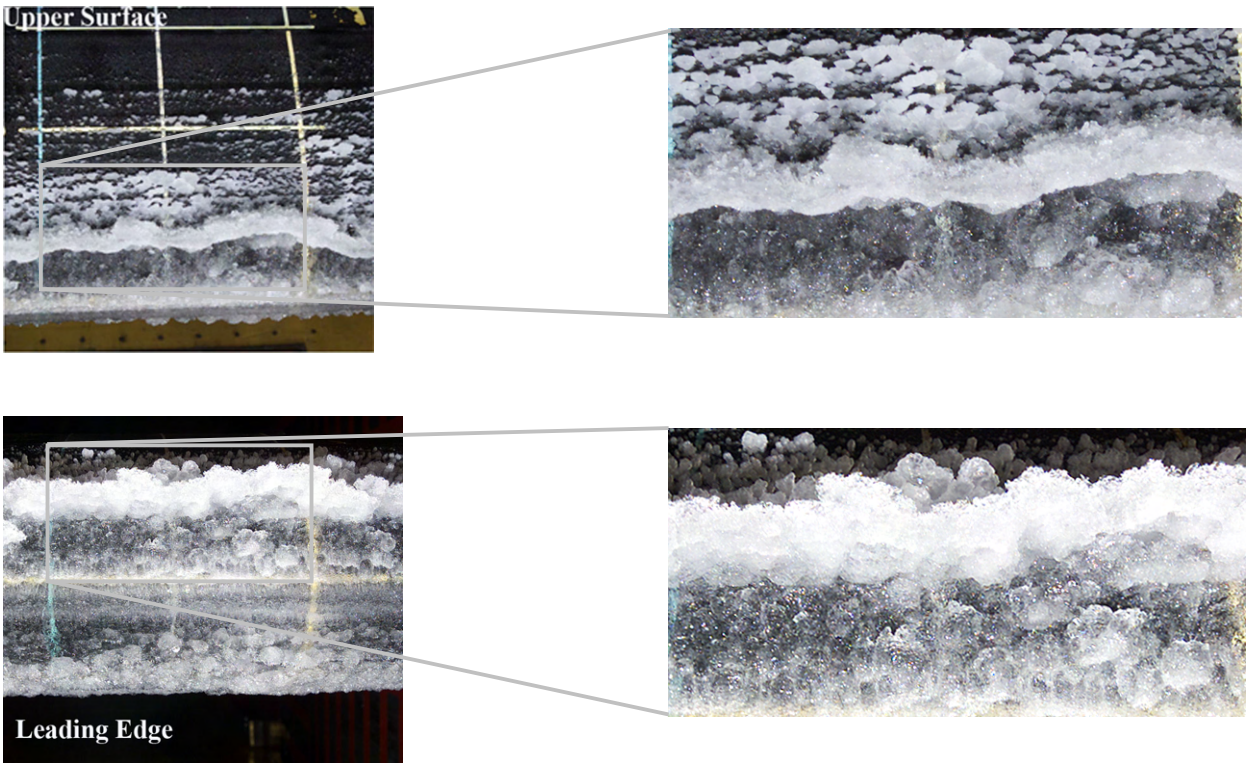

Figure 3. Close-up photographs of SLD horn features.

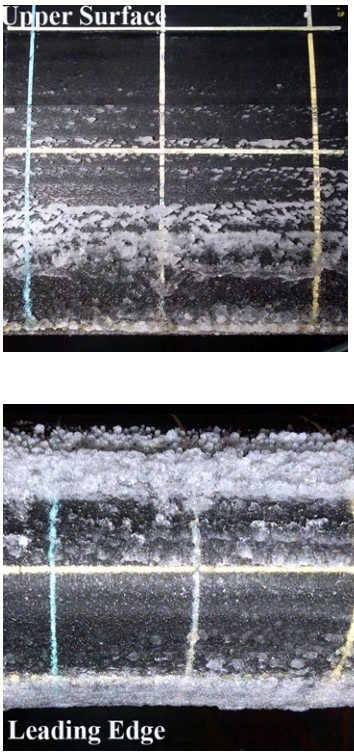

Run	Velocity (kts)	Angle of Attack (deg.)	Total Temp. (°F)	*MVD* (μm)	*LWC* (g/m^3)	Spray Time (min.)
583	180	3	28.0	133	0.32	10.0

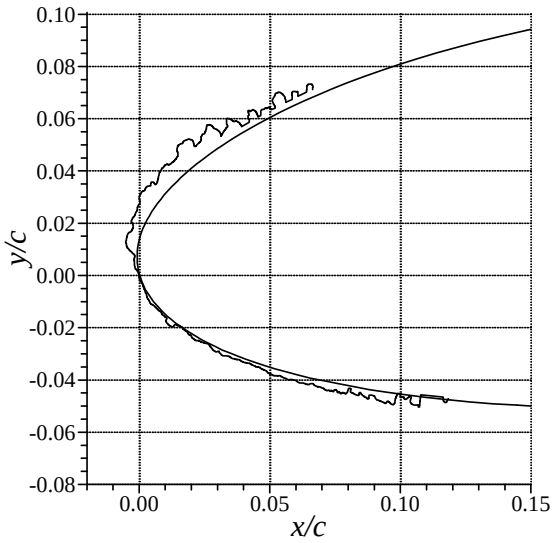

Figure 4. SLD ice accretion having identical conditions to that in Fig. 2, but with a shorter spray time.

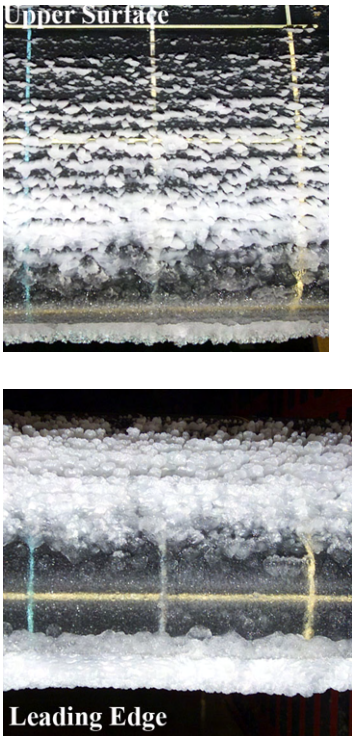

Run	Velocity (kts)	Angle of Attack (deg.)	Total Temp. (°F)	*MVD* (μm)	*LWC* (g/m^3)	Spray Time (min.)
591	180	-1	21.9	133	0.32	10.6

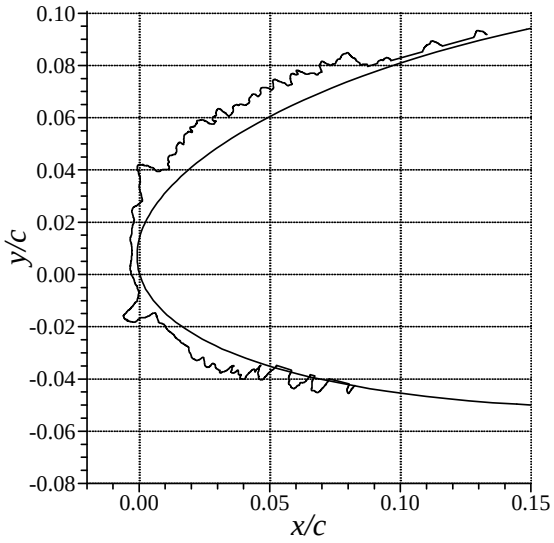

Figure 5. SLD ice accretion for -1 deg. angle of attack.

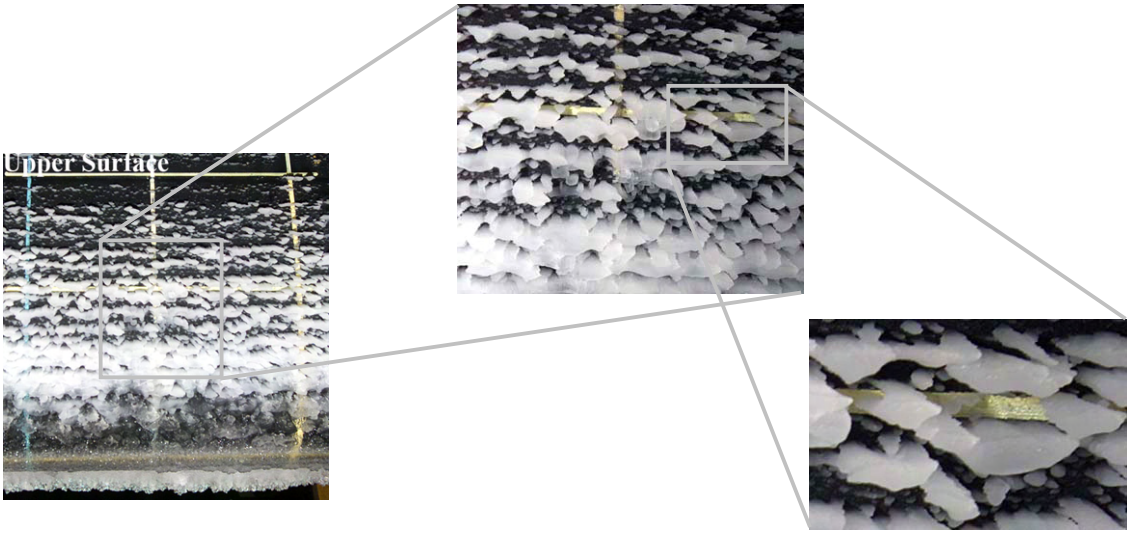

Figure 6. Close-up photographs of SLD nodule features.

For the conditions run in this test, the clear ice feature was always located at the airfoil leading edge, including the stagnation region. As shown in Fig. 7, this feature was a glaze ice formation having a clear color and a relatively smooth, conformal surface. The composition of the clear ice transitions to mixed ice between the stagnation region of the clear ice and the limits of the clear ice feature. This location also coincided with the smooth/rough boundary.[15] That is, the formation of the nodule and horn features occurred downstream of this boundary. The thickness of the ice in this region followed predictable trends based upon the local collection efficiency, airspeed and cloud *LWC*.

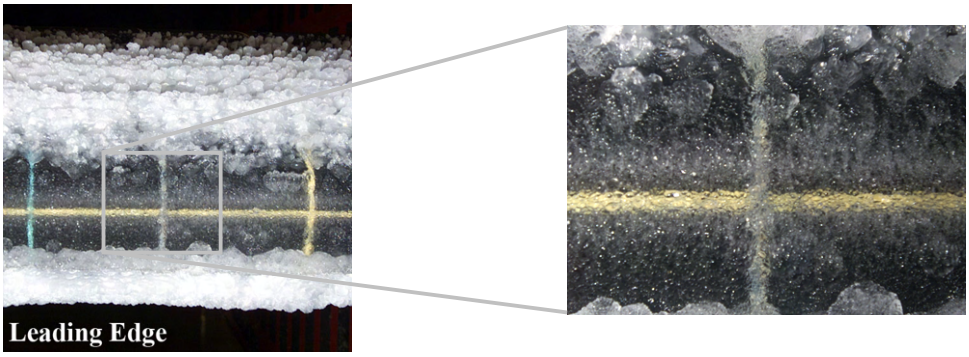

Figure 7. Close-up photograph of SLD clear ice feature.

An additional objective of this study was to generate SLD ice accretions that were representative of in-flight SLD accretions. However, comparison of tunnel-generated accretions with in-flight accretions is complicated by several factors. The most important of these is that flight data were only available for a few cases. Secondly, these data indicated that the in-flight cloud *LWC*s may be lower than could be obtained in the tunnel. An attempt to address this was made by scaling the conditions to simulate lower *LWC*s. A third complication is that real SLD clouds may be composed of both large and small droplet distributions. This is presently being addressed in other research.[16,17] A summary of the scaled *LWC* conditions is given in Table 1. One scale run was performed at 180 kts and three scale runs were performed at 120 kts. For each case, the reference condition lists an *LWC* value lower than the IRT operational value. The temperature and spray time were adjusted in each of the corresponding scale cases to match the freezing fraction and accumulation parameter. This resulted in lower temperatures and spray times from the reference conditions.

Table 1. Summary of Scale Conditions

Condition	Run	Velocity (kts)	Angle of Attack (deg.)	Total Temp. (°F)	*MVD* (μm)	*LWC* (g/m^3)	Spray Time (min.)	Freezing Fraction	Accum. Parameter
Reference	-	180	3	28.0	133	0.15	22.5	0.36	0.21
Scale	585	180	3	21.9	133	0.32	10.6	0.36	0.21
Reference	-	120	3	29.4	133	0.20	22.5	0.20	0.18
Scale	577	120	3	24.6	133	0.55	8.2	0.20	0.18
Reference	-	120	3	29.4	133	0.15	22.5	0.26	0.14
Scale	578	120	3	22.2	133	0.55	6.1	0.26	0.14
Reference	-	120	3	29.4	133	0.10	22.5	0.37	0.09
Scale	579	120	3	16.6	133	0.55	4.1	0.37	0.09

Since it was impossible to run the reference case in the IRT, it was difficult to assess the effectiveness of the scaling method. Only relative comparisons were made. The results of scale run 578 (cf. Table 1) are shown in Fig. 8 and these were compared with the results of run 575 in Fig. 9. The reference conditions for Fig. 8, are identical to that in Fig. 9, except that the *LWC* was 0.15 g/m^3 instead of 0.55 g/m^3. So, if the scaling was fully effective these figures would illustrate the effect of lower *LWC*. As expected, the total mass of ice in Fig. 8 is less than in Fig. 9, owing to the shorter spray time, or interpreted in terms of the scaling, lower effective *LWC*. The ice limits were very similar since the *MVD* was identical. The characteristics of the nodules, being smaller in size in Fig. 8 also probably reflect lower *LWC*. A major difference, however, is the surface extent of the clear ice region. This is much larger in Fig. 8 than in Fig. 9. This could have been caused by the lower temperature in the scaled case. It is uncertain if a lower *LWC* would cause the clear ice region to be larger at a smaller *LWC*, but same temperature.

A similar comparison is shown in Fig. 10 for scale run 585. This accretion can be compared to run 593, already plotted in Fig. 2. As for the previous case, the ice limits are similar, and the scale conditions does appear to have less total ice. The ice horn, in particular, is smaller in Fig. 10 than in Fig. 2. While this is consistent with a lower *LWC*, the horn location being closer to the leading edge in Fig. 10 may be due to the lower temperature. More research is required to help identify the complex interactions among the icing parameters. Overall, the scaled runs showed some promise in capturing the essential ice features resulting from lower-*LWC* icing clouds.

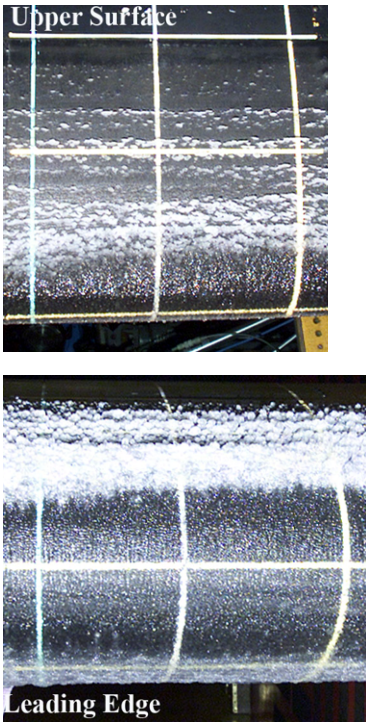

Run	Velocity (kts)	Angle of Attack (deg.)	Total Temp. (°F)	*MVD* (μm)	*LWC* (g/m^3)	Spray Time (min.)
Reference	120	3	29.4	133	0.15	22.5
578 Scale	120	3	22.2	133	0.55	6.1

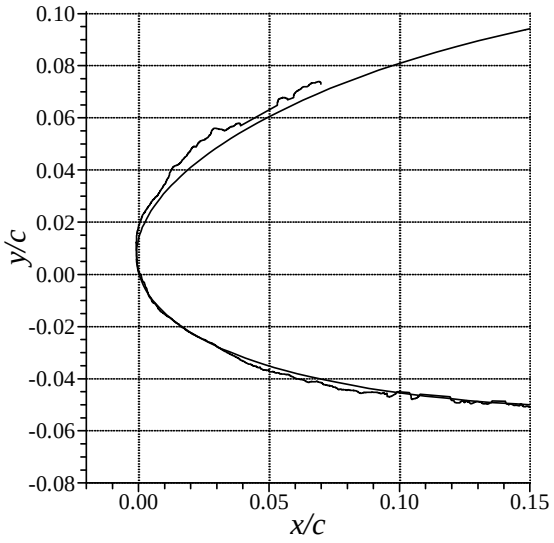

Figure 8. Photographs and tracing for scale run 578.

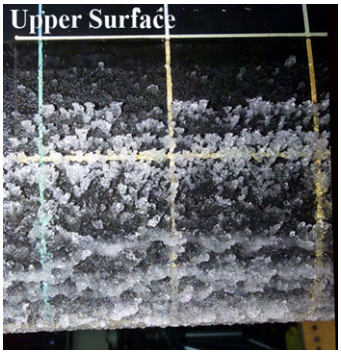

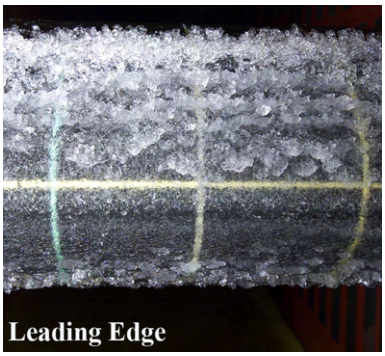

Run	Velocity (kts)	Angle of Attack (deg.)	Total Temp. (°F)	*MVD* (µm)	*LWC* (g/m^3)	Spray Time (min.)
575	120	3	29.4	133	0.55	22.5

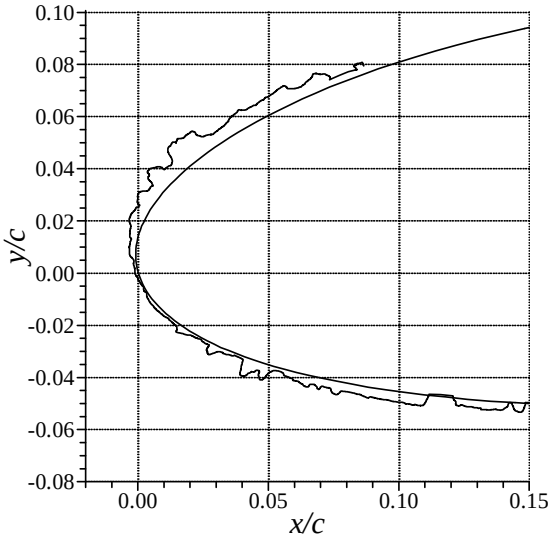

Figure 9. Photographs and tracing for run 575.

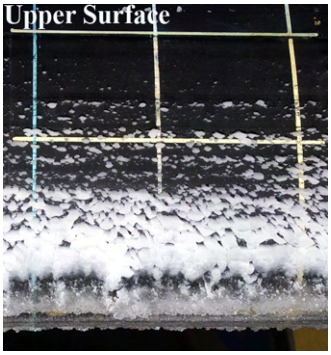

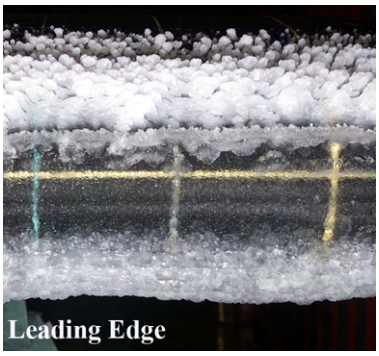

Run	Velocity (kts)	Angle of Attack (deg.)	Total Temp. (°F)	*MVD* (µm)	*LWC* (g/m^3)	Spray Time (min.)
Reference	180	3	28.0	133	0.15	22.5
585 Scale	180	3	21.9	133	0.32	10.6

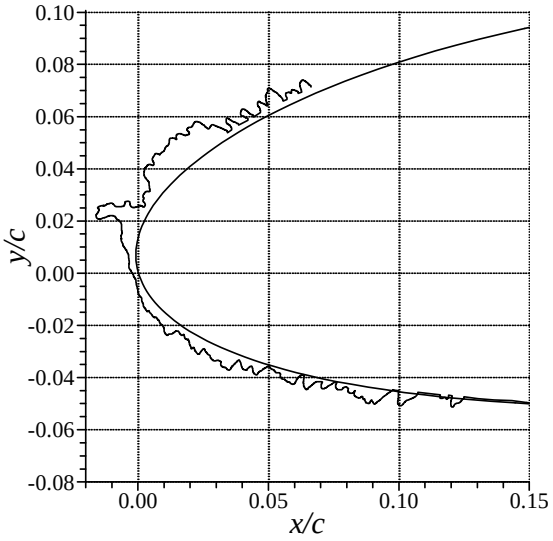

Figure 8. Photographs and tracing for scale run 585.

This summary of the SLD ice characterization testing has led to the identification of some key characteristics for the conditions tested. Therefore, a comparison to in-flight SLD ice accretion data is warranted. Figures 11 and 12 show a picture and ice tracing obtained from separate flights of NASA Glenn Research Center's Twin Otter Icing Research Aircraft. This aircraft is specifically instrumented for gathering in-flight atmospheric and ice accretion data. The photograph in Fig. 11 shows some qualitative similarities with the ice features identified here. It appears that horns have begun to form on both the upper and lower surface side of the clear ice region near the stagnation zone. Small nodules also seem to be present downstream of the horns. The corresponding tracing was produced from post-processing of a stereo image like the one to the left of the tracing. It shows that the thickest ice is nearest the stagnation point in the clear ice region. This is different from the ice characteristics in the IRT results. This difference could be due, in part, to the impingement of smaller droplets resulting from the bi-modal characteristics of natural SLD clouds. The photograph in Fig. 12 shows an SLD accretion with a clear ice region that transitions to nodules without any evidence of horn features. This type of accretion is analogous to that shown in Figs. 8 and 9. As in Fig. 11, the tracing obtained from the stereo images shows the location of maximum ice thickness (or height) to be near the stagnation point. However, the photograph seems to indicate that the upper surface nodules do have a height comparable to this. This may be a limitation of the stereo image processing method since the upper surface locations appear "flat" relative to the image plane. Overall, there is good qualitative agreement between the in-flight ice accretion characteristics and those obtained from the icing-tunnel.

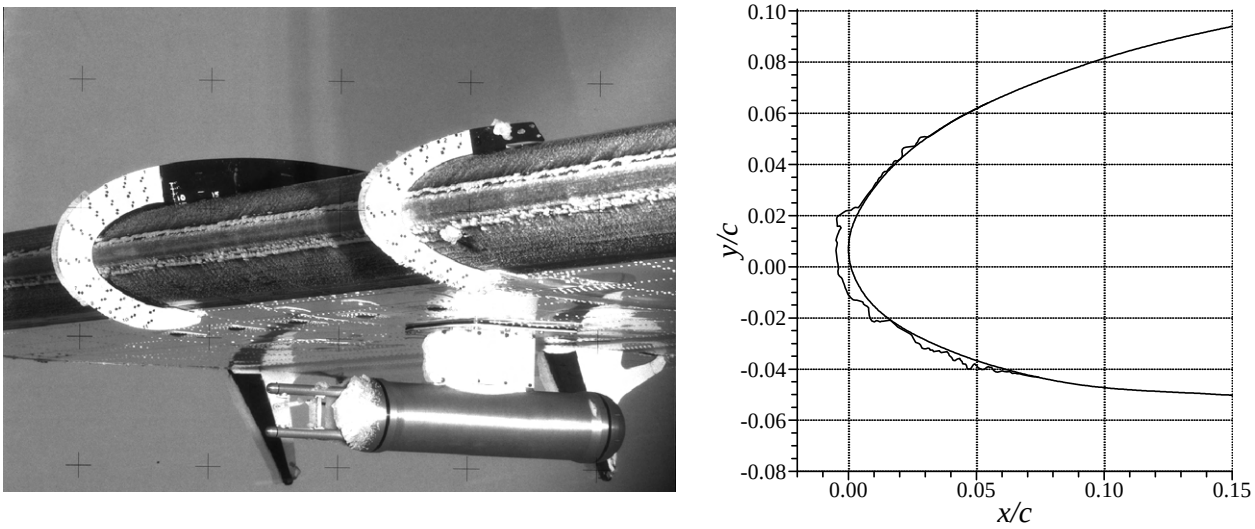

Figure 11. Photograph and tracing from December 1997 Twin Otter flight.

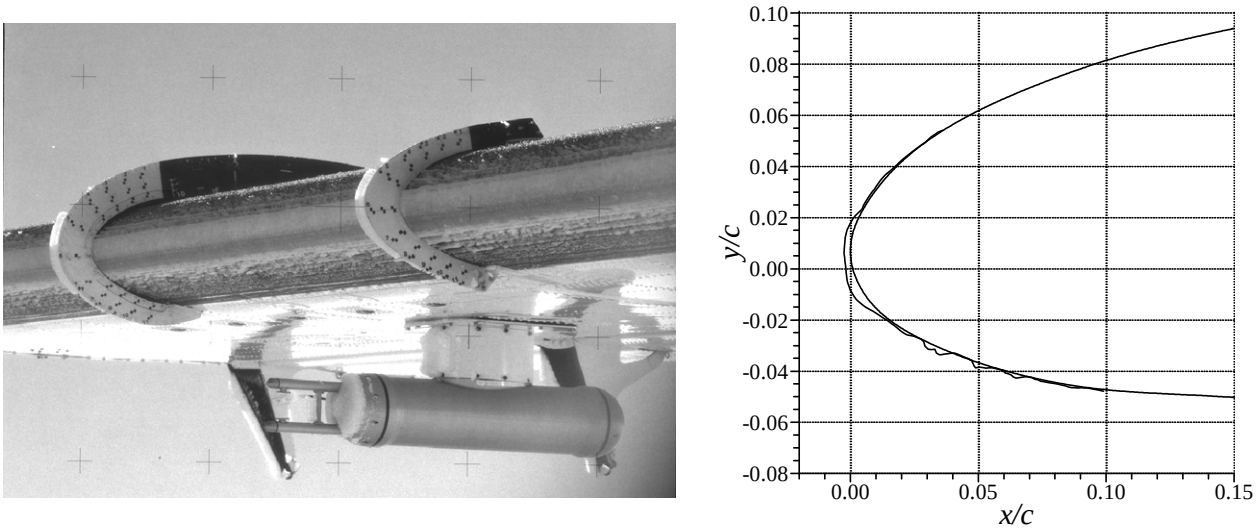

Figure 12. Photograph and tracing from February 1998 Twin Otter flight.

III. Aerodynamic Testing

A. Experimental Methods

The second part of this study was performed at the Subsonic Aerodynamics Laboratory at the University of Illinois. The low-speed, low-turbulence wind tunnel was an open return type with a working section 2.8-ft high, 4-ft wide and 8-ft long. The 18-inch chord aerodynamic model spanned the full height of the test section and had the same commuter airfoil section as the IRT icing model. The model had a total of 85 surface pressure taps. There were 73 chordwise taps and 12 spanwise taps. A three-component force balance was used to measure the lift and pitching moment on the airfoil as well as to set the angle of attack. The force balance was located below the test section and supported the model. This arrangement is shown in Fig. 13. Also depicted is the traversable wake rake with 59 total-pressure tubes that was used to obtain the airfoil drag. Both the wake pressures and the model surface pressures were measured with an electronically scanned pressure (ESP) system. More details about this experimental apparatus can be found in Lee.[18]

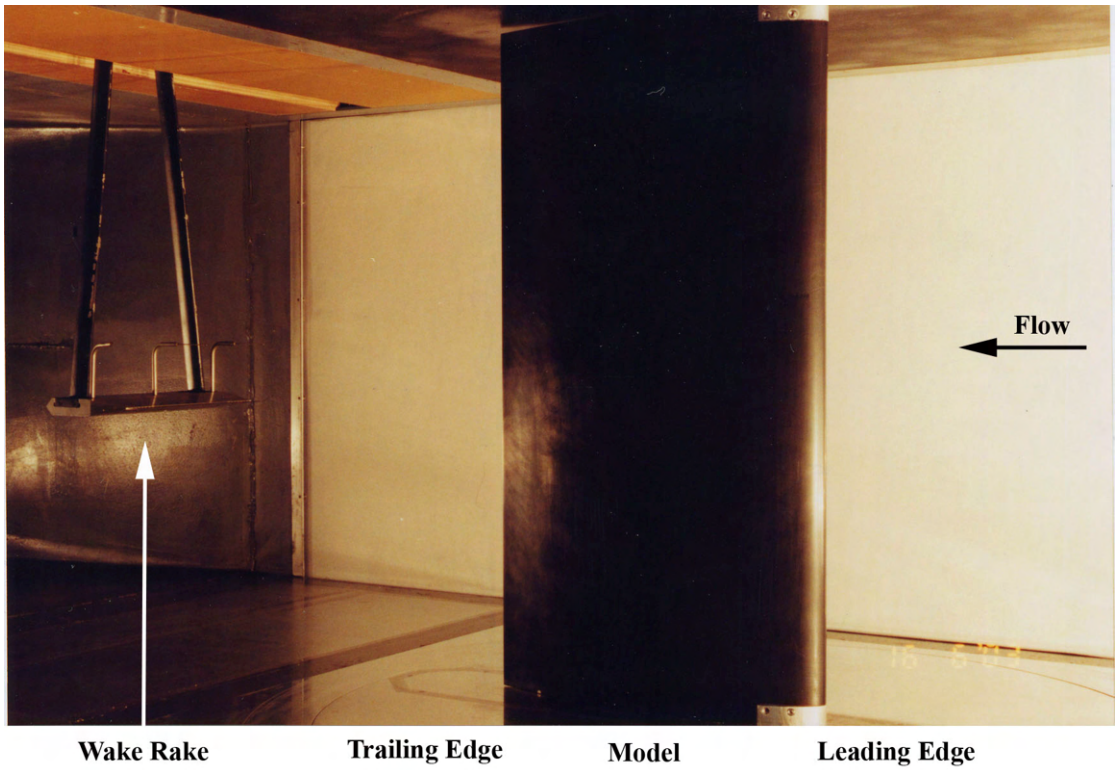

Figure 13. Experimental set-up for aerodynamic testing.

The lift coefficient and quarter-chord pitching-moment coefficient were derived from both the force-balance and the surface-pressure measurements. The agreement in the results from these two methods was very good for the clean model configuration. Larger differences were observed for the iced-model configurations because surface pressures could not be measured accurately in the vicinity of simulated ice accretions. Therefore, the lift data and pitching-moment data presented here were taken from the force-balance measurements. The drag coefficient was calculated from the wake pressures using standard momentum-deficit methods. All of these aerodynamic coefficients and the angle of attack were corrected for wall interference effects using the methods of Rae and Pope.[19] The experimental uncertainty in these coefficients was also estimated using the methods of Kline and McClintock[20] and Coleman and Steele[21] for 20:1 odds (see Table 2). The uncertainties in α, C_l and C_m were determined from the force-balance data and the remaining quantities (C_p, C_d) were determined from the pressure-based data. The values were determined by Lee[18] and Lee and Bragg[22] for freestream conditions of $Re = 1.8\times10^6$ and $Ma = 0.18$. All data reported in this paper correspond to this freestream condition.

Table 2. Estimated Experimental Uncertainties

Aerodynamic Quantity	Reference Value	Absolute Uncertainty	Relative Uncertainty
α	5.00	±0.02	±0.40%
C_p	-0.712	±0.0037	±0.52%
C_l	0.295	±0.0016	±0.53%
C_m	-0.0791	±0.00039	±0.50%
C_d	0.0102	±0.00014	±1.40%

The ice accretion simulations consisted of simple geometric shapes that represented the actual features found on the SLD accretions. The baseline size of these features were taken from the icing test results and scaled down by the ratio of the model chord lengths (i.e., 18.0/77.25). This geometric scaling method has been employed successfully in other studies where the size of the ice accretion is large relative to the local boundary-layer thickness.[23,24] Parametric variations in the size of these features were also tested to gauge the aerodynamic sensitivity. The nodules were simulated using various hemispherical shapes with different patterns and densities. Table 3 lists the dimensions of four different nodule sizes tested. The smallest size (k/c = 0.0012) was constructed by relief punching the hemispherical shape into a vinyl tape strip having a thickness of 0.003-inch (k/c = 0.00017). The k/c = 0.0026 nodule simulations were composed of faceted plastic hemispheres while the two largest sizes were smooth plastic hemispheres. The sizes listed for these plastic hemispheres is the average of a random sampling as there were small variations in the size of the individual pieces. The plastic hemispheres were attached to the airfoil model using 0.003-inch (k/c = 0.00017) thick double-sided tape. Two nodule patterns were chosen for the simulations: offset and aligned. These were selected to capture the extent of the variations from the ice accretions and are shown in Fig. 14. The clear ice simulations were constructed from a flexible plastic casting with three different roughness patterns of varying thickness. The surface extent of the clear ice simulation was also varied. These were attached to the model surface using 0.003-inch (k/c = 0.00017) thick double-sided tape. The dimensions are summarized in Table 4 and the patterns are illustrated in Fig. 15. The horn shapes were constructed from balsa wood, cut to the sizes shown in Fig. 16. The horn simulations had no spanwise variation in these tests.

Table 3. Simulated Nodule Characteristics

Nodule Simulation (Hemispherical)	Mean Diameter (inch)	Mean Height, k (inch)	Normalized Height, k/c
Punched Vinyl	0.041	0.021	0.0012
Faceted Plastic	0.118	0.046	0.0026
Smooth Plastic	0.194	0.102	0.0057
Smooth Plastic	0.271	0.113	0.0063

Table 4. Simulated Clear Ice Characteristics

Clear Ice Simulation Roughness Pattern	Mean Height, k (inch)	Normalized Height, k/c
Smooth	0.040	0.0022
Medium	0.056	0.0031
Rough	0.078	0.0043

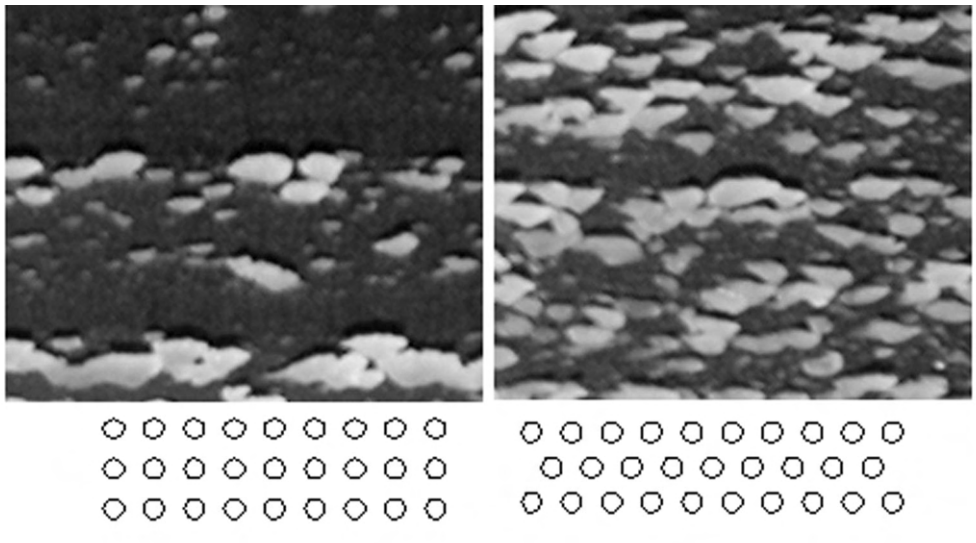

Figure 14. Comparison of aligned nodule simulation pattern (left) with offset pattern.

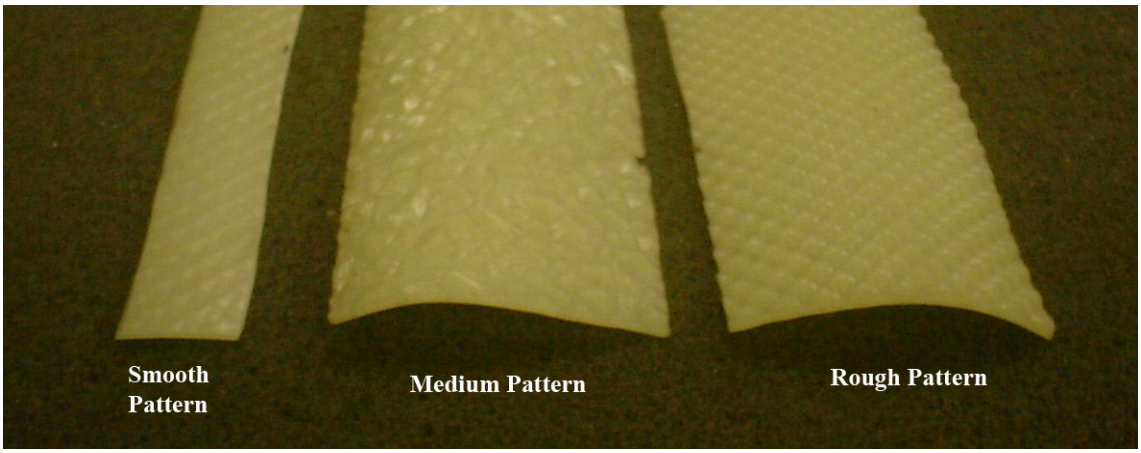

Figure 15. Comparison of the clear ice simulation roughness patterns.

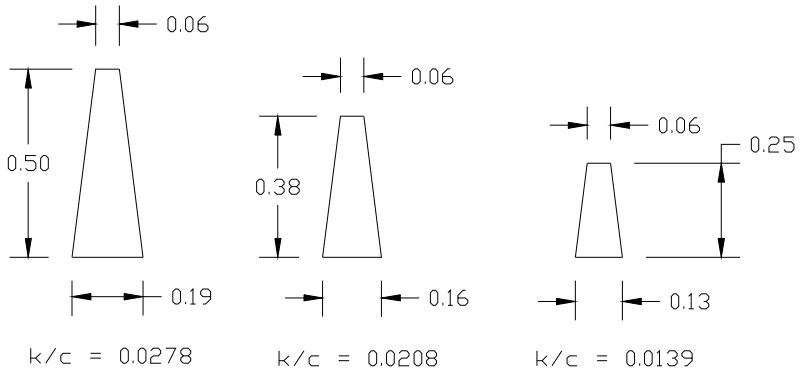

Figure 16. Sketches of horn simulations (dimensions in inches).

The aerodynamic performance testing was conducted in two phases. The first phase involved testing of the individual ice feature simulations. For example, angle-of-attack sweeps were performed with only nodule simulations applied to the airfoil model. These tests investigated the effect of nodule size, spacing, pattern, etc. Other tests were performed with only the clear ice simulations applied to the model leading edge. The three sizes of horn simulations were also tested in various combinations of upper and lower surface locations without any of the other ice simulations. In the second phase of the aerodynamic testing, these individual features were combined to represent certain SLD ice accretions. Two general patterns, with and without horns, are illustrated in Fig. 17. Both categories of simulations were composed of a selected clear ice simulation, with various nodule sizes and patterns located downstream on the upper and lower surface, as in the actual ice accretion. Some cases also include horn simulations located in the appropriate location on the upper and/or lower surface, depending upon the nature of the actual ice accretion. An example of a combination of these ice feature simulations as installed on the model is shown in Fig. 18. The clear-ice simulation was located on the leading-edge in the area of the stagnation point. A horn simulation was located downstream on the upper surface. Nodule simulations were located downstream on the lower surface. The upper surface nodules were located downstream of the horn and are not visible in the picture.

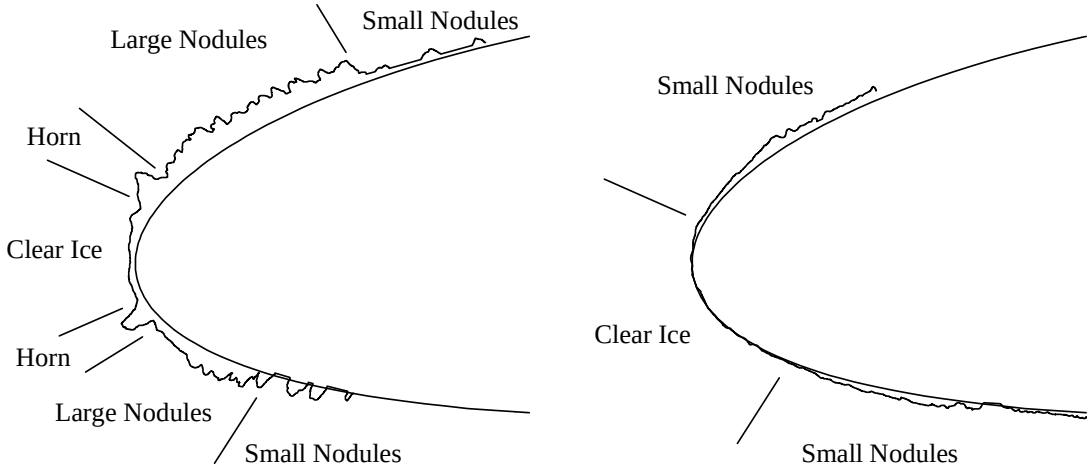

Figure 17. General SLD ice accretion patterns; with horns (left) and without horns.

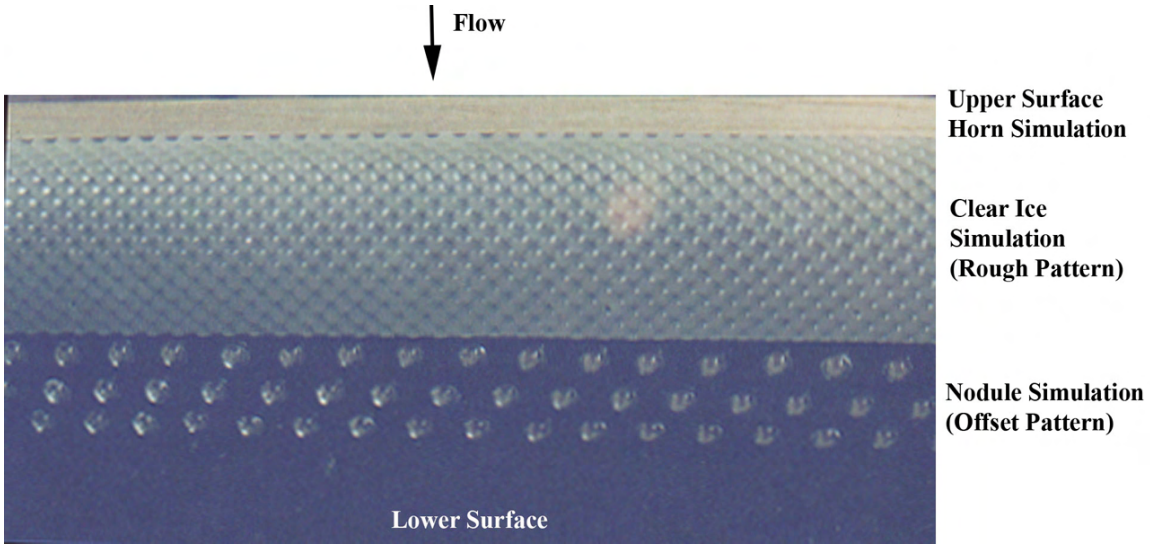

Figure 18. Combination of individual SLD ice feature simulations applied to the aerodynamic model.

B. Results and Discussion

In the first test phase, aerodynamic performance measurements were carried out with each of the three ice feature simulations applied to the model separately. The objective of this test phase was to evaluate the aerodynamic effect of each feature in isolation. For example, the nodule simulations listed in Table 3 were applied to the model upper surface in various combinations. The spacing of the individual hemispheres was expressed in terms of the center-to-center distance and alignment pattern. Figure 19 shows the effect of the alignment pattern on the airfoil lift and pitching moment for the k/c = 0.0057 hemispheres spaced two diameters (2-D) apart and located at x/c = 0.026 to 0.076 on the upper surface. This range of x/c corresponded to approximately one-inch of surface arc length. For this size hemisphere, three rows were applied over this range of surface distance. The plot shows that the difference in lift and pitching-moment coefficient between the offset and aligned patterns near stall was small relative to the departure from the clean values. Similar differences in the drag coefficient (not shown) were also observed. In reality the nodules did not organize themselves into uniform rows. These data show that the alignment does not have a large impact on the integrated aerodynamics.

The effect of nodule size and number density were also investigated and these results are shown in Fig. 20. The chordwise location and spacing of the hemispheres was identical to Fig. 19 and all cases had an offset spacing. The number of hemisphere rows was limited to four (4) for k/c = 0.0011, owing to the fabrication method. The numbers of rows for the remaining hemisphere sizes was limited, since the chordwise extent was held constant across the range of simulations. The data reflected this trade-off in simulated nodule size versus the number of rows. For hemispheres with k/c s, not the increase in disturbance height. For angles of attack less than about 6 deg., there were only small differences in the lift and pitching moment across the range of sizes. This was also true for the drag, with the exception of the smallest size. The increase in drag coefficient from the clean case for $\alpha > 6$ deg. was largest for the nodule simulation with the largest number of rows. The next highest increase in drag was caused by the largest size nodule simulation with the fewest number of rows, further illustrating the trade-off in these parameters. The effects of hemisphere number density on lift and drag are more clear when compared at a constant disturbance height. As expected, the data in Fig. 21 show that the larger degradation in lift and drag occurred for the nodule simulation with the larger number of elements.

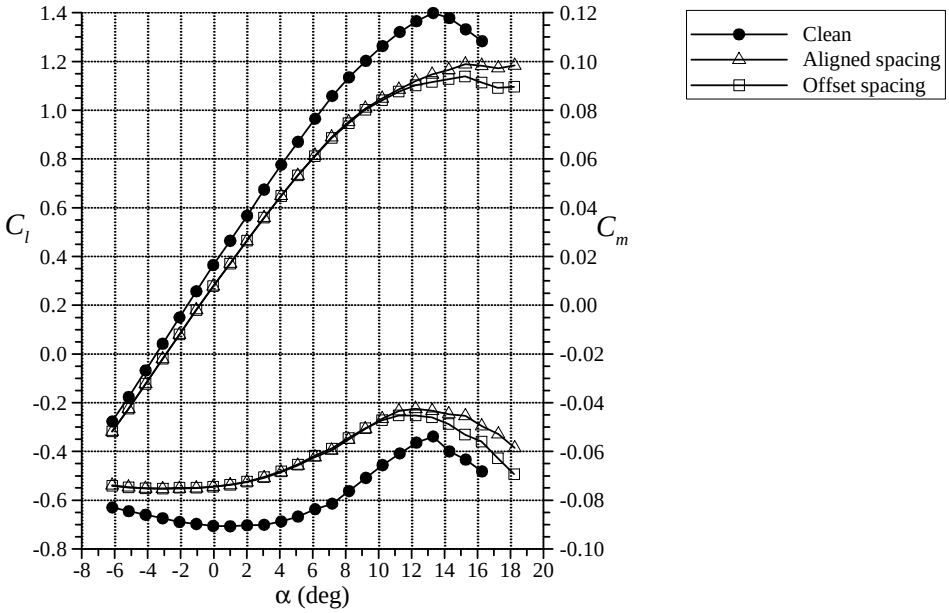

Figure 19. Aerodynamic performance effects of nodule simulation pattern with k/c = 0.0057 located at x/c = 0.026 to 0.076 on the upper surface, 2-D spacing.

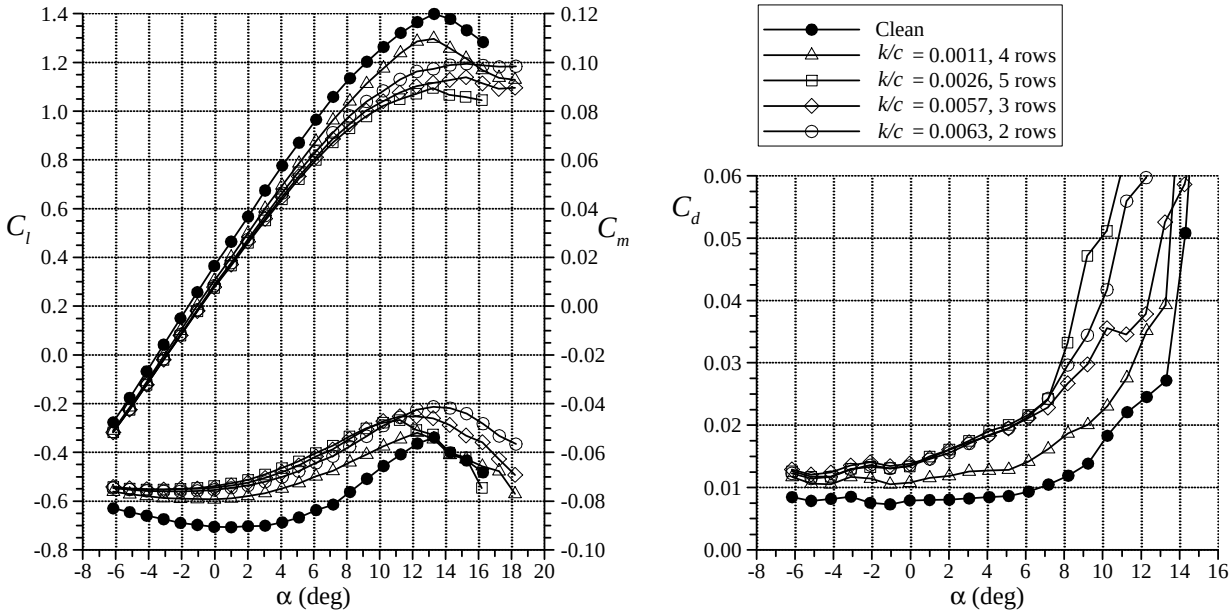

Figure 20. Aerodynamic performance effects of nodule simulation size and number density located at *x*/*c* = 0.026 to 0.076 on the upper surface, 2-D offset spacing.

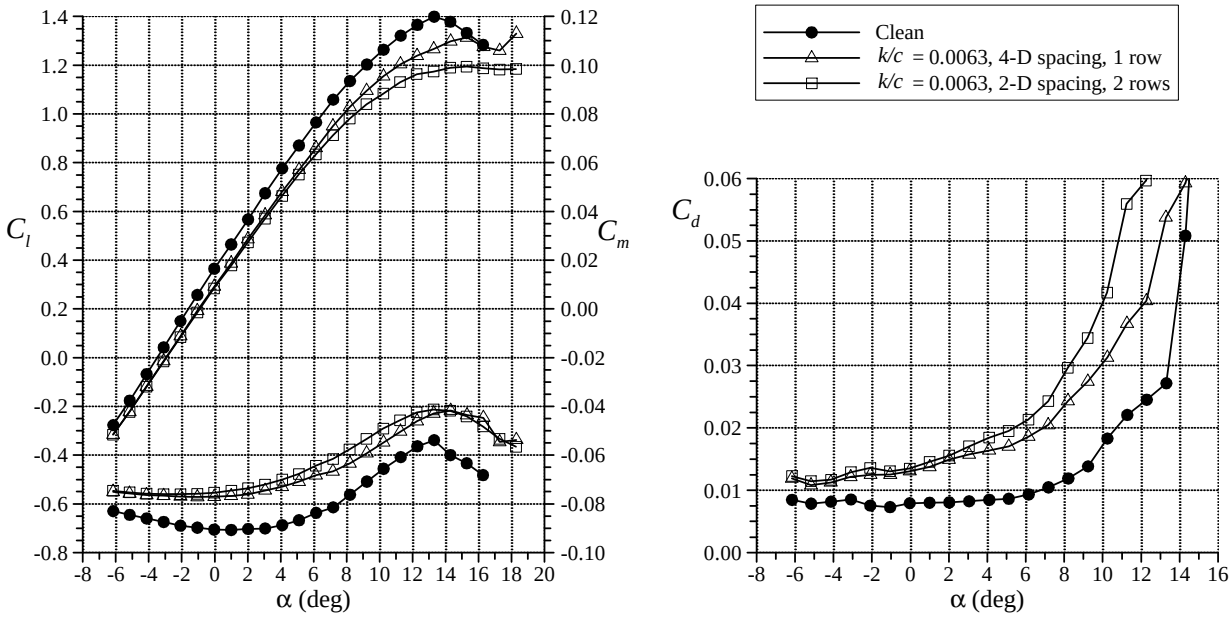

Figure 21. Aerodynamic performance effects of nodule simulation number density located at *x*/*c* = 0.026 to 0.076 on the upper surface, offset spacing.

The effect of nodule surface location was also investigated. Some sample results are shown in Fig. 22 for *k*/*c* = 0.0057 hemispheres with 2-D offset spacing. The surface coverage of the nodule simulation was the same for both cases, with the difference in *x*/*c* spacing resulting from the airfoil curvature. The plot shows a significantly larger reduction in maximum lift with the simulated nodules located closer to the leading edge. This effect of disturbance location is consistent with the well known plot of Brumby.[25] In fact, the maximum lift penalties shown here, on the order of 20 to 25% of the clean value, fall close to the range predicted by Brumby for disturbances of this size. Comparisons to the Brumby plot should be performed with caution, as Lee and Bragg[6] have shown that more significant maximum lift penalties can occur with simulated ice located farther downstream.

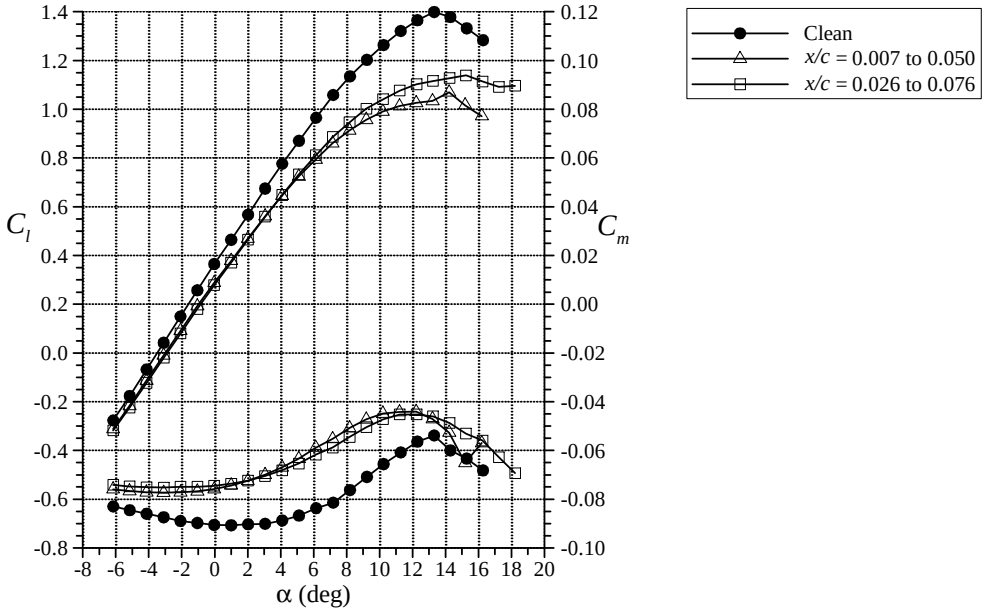

Figure 22. Aerodynamic performance effects of nodule simulation surface location with *k/c* = 0.0057, 2-D offset spacing, 3 rows.

The clear ice simulations tested in isolation on the airfoil leading edge, resulted in similar performance effects. As shown in Fig. 23, the maximum lift decreased with increased disturbance height and roughness level. The $C_{l,max}$ values, in the range of 1.05 to 1.15, were similar to those with the nodule simulations. The effect of surface extent of the clear ice simulation is given in Fig. 24. The results were also analogous to the nodule simulation data. The larger surface coverage led to larger performance penalties in terms of decreased lift and increased drag. The amount of parametric testing of the clear ice simulations was limited by the inability to fabricate multiple size and roughness combinations. In spite of this, the range tested did represent the ice accretions documented during the IRT test phase.

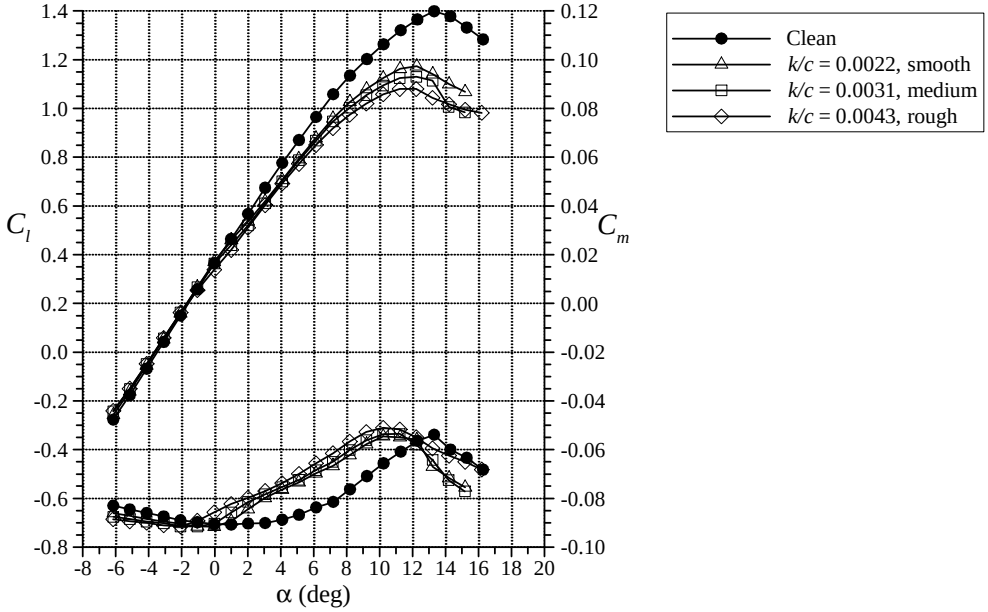

Figure 23. Aerodynamic performance effects of three clear ice simulations; all located at *x/c* = 0.006 on the lower surface to 0.000.

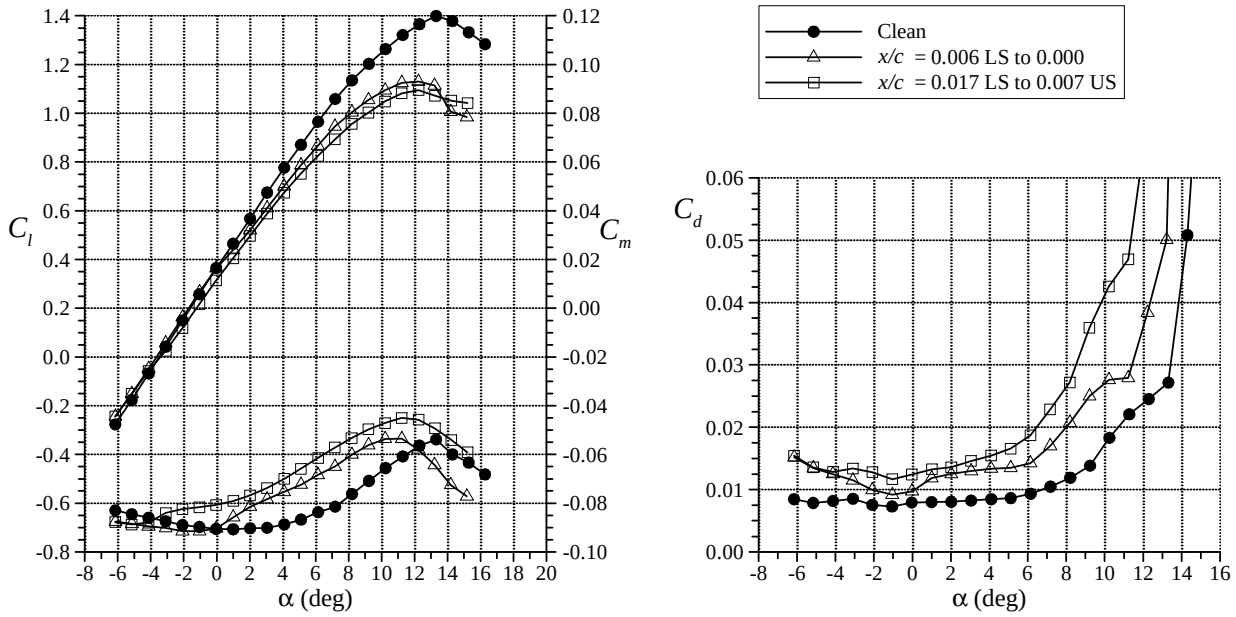

Figure 24. Aerodynamic performance effects of clear ice simulation surface extent with *k*/*c* = 0.0031, medium roughness.

The array of horn simulations shown in Fig. 16 were tested at several upper and lower surface locations on the airfoil, based upon the documented ice accretions. Typical effects were observed where the larger size horns located farther downstream caused the largest degradations in aerodynamic performance. These results were consistent with analogous work in other studies.[26,27] Sample results are shown in Fig. 25 for the smallest (k/c = 0.0139) horn simulation located on the upper surface, with and without an identical lower surface horn simulation. The horn simulations had a much larger effect on the aerodynamics than the nodule or clear ice simulations. The $C_{l,max}$ values in the latter cases generally ranged from 1.05 to 1.15. Here, $C_{l,max}$ was less than 0.80 for the smallest size horn simulation. Figure 25 also shows the contribution of the lower surface horn to the aerodynamic penalty. Its effect was largest in the negative stall region. For angles of attack larger than -3 deg., the effects of the lower surface horn began to diminish in the lift and pitching-moment while the drag curves converged at about α = 6 deg. The effect of upper surface horn size (with lower surface horn) is shown in Fig. 26. The lift values near stall at negative angle of attack were unaffected by the difference in upper surface horn height. However, there was a more pronounced effect on the pitching moment and drag. For positive angle of attack, the larger upper surface horn reduced the $C_{l,max}$ value to approximately 0.50, thus illustrating the dominant effect that the horn shapes had on the aerodynamics.

In the second phase of aerodynamic testing, these individual ice feature simulations were combined to simulate complete SLD ice accretions. The objective was to determine the overall aerodynamic penalties associated with a complete accretion and determine which of the three features played an important role in the resulting penalties. Following the categories suggested in Fig. 17, this discussion is divided into simulated SLD accretions with horns and those without horns. The classification is based upon that fact horn features, when present, tended to dominate the aerodynamics.

Complete SLD accretions were simulated with various combinations of the individual key features. The details of the "baseline" ice simulation are given in Table 5. The aerodynamic effect of the baseline ice simulation is shown in Fig. 27 as compared to the effect of only the upper surface horn present on the airfoil surface. The maximum lift value for the baseline simulation was approximately 0.70, thus indicating the dominating presence of the horn ice feature. However, the data also show that this value of $C_{l,max}$ was higher than the value obtained when only the horn feature is simulated. This means that the addition of the other ice features improved the maximum lift characteristics. The drag data indicated a mixed result. That is, for angles of attack less than 0 deg., the baseline ice simulation had higher drag than for the airfoil with only the horn simulation. For angles of attack higher than 0 deg., the opposite was true.

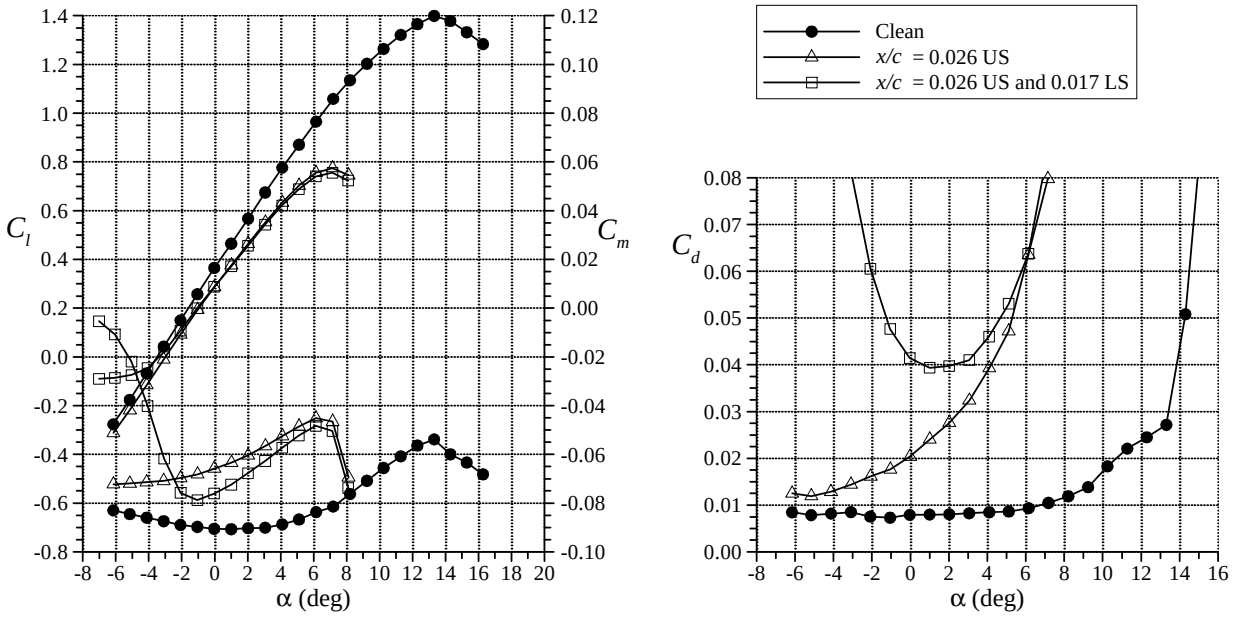

Figure 25. Aerodynamic performance effects of horn simulations with *k/c* = 0.0139 for each horn.

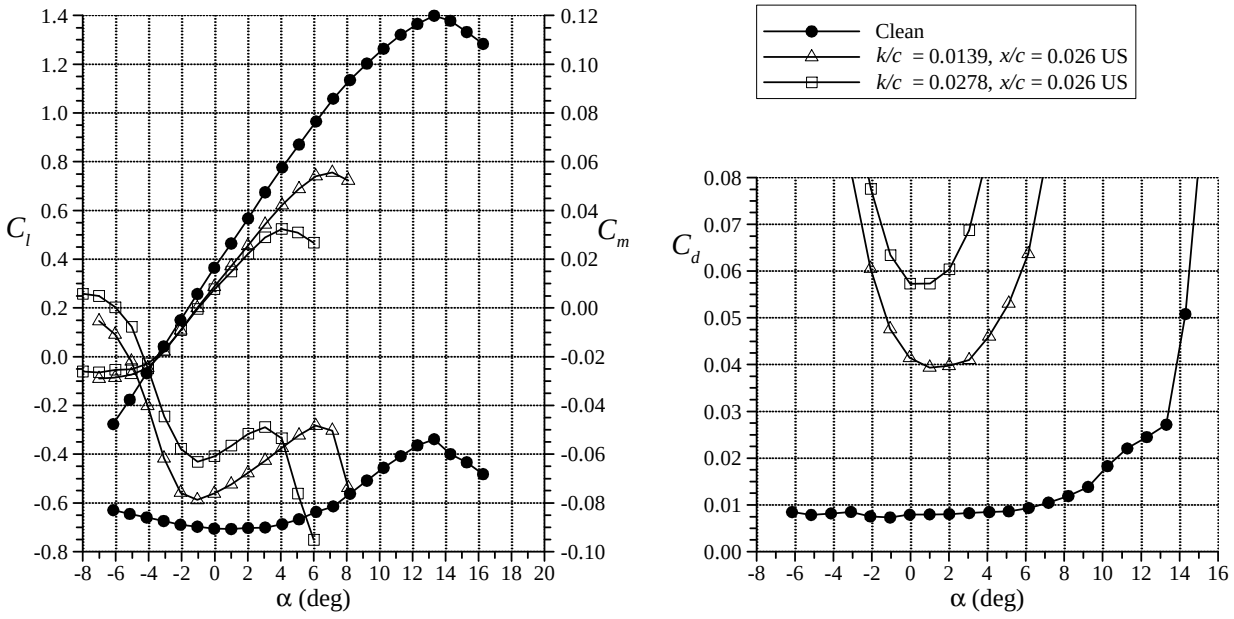

Figure 26. Aerodynamic performance effect of upper surface horn simulation height with *k/c* = 0.0139 lower surface horn located at *x/c* = 0.017.

Table 5. Baseline Ice Simulations for Figs. 27 and 28.

Lower Surface Nodule Simulation	Lower Surface Horn Simulation	Clear Ice Simulation	Upper Surface Horn Simulation	Upper Surface Nodule Simulation
k/c = 0.0057, from x/c = 0.042 to 0.096 2-D offset spacing	None	k/c = 0.0031 from x/c = 0.042 LS to 0.006 US	Fig. 27: k/c = 0.0278 at x/c = 0.016 Fig 28: k/c = 0.0139 at x/c = 0.016	k/c = 0.0057, from x/c = 0.026 to 0.074 2-D offset spacing

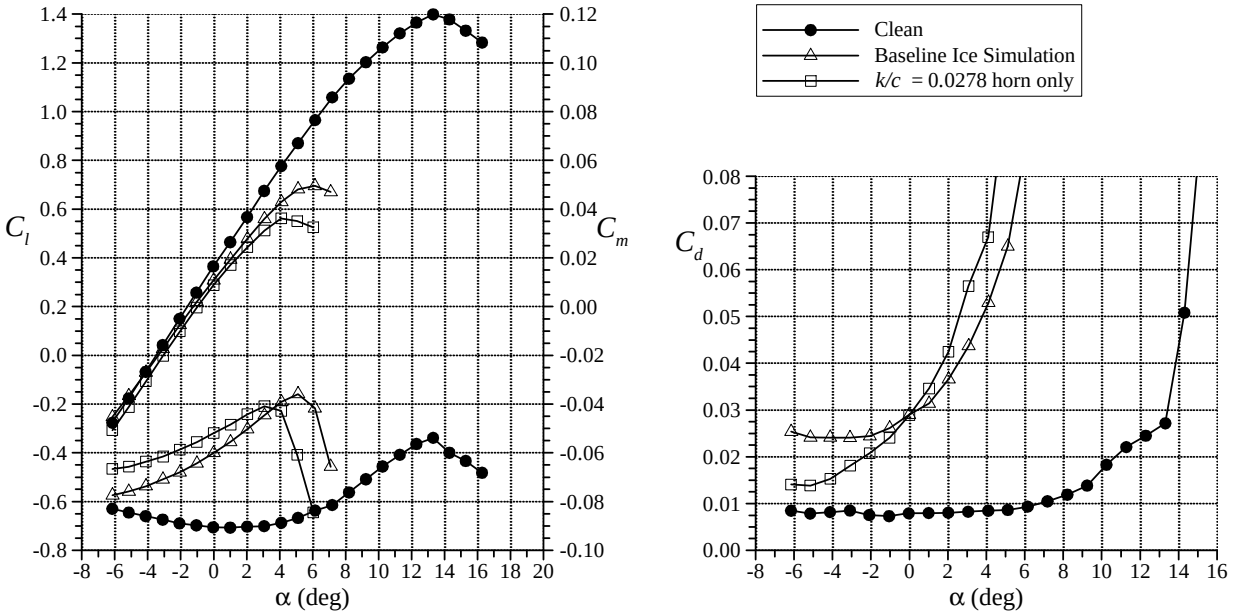

Figure 27. Aerodynamic performance comparison of the baseline SLD ice accretion simulation with the horn-only case (cf. Table 5).

The improvement in maximum lift for the baseline simulation over the horn-only case was likely caused by the presence of the simulated clear ice upstream of the horn. The horn height was smaller when referenced to the surface of the clear ice, than when referenced to the airfoil surface. This would tend to lessen the separation region aft of the horn and improve performance. A comparison of the pressure distributions for these cases indicated that the separated flow region aft of the horns was larger for the horn-only case.

The effect of the relative height of the clear ice and horn simulations is further illustrated in Fig. 28. In this example, the baseline simulation was the same as in Fig. 27 except that the horn simulation was reduced in size to k/c = 0.0139. There was also an improvement in $C_{l,max}$ over the horn only case and the drag characteristics also followed a pattern similar to Fig. 27. Increasing the height of the clear ice simulation resulted in an additional increase in $C_{l,max}$ and decrease in drag for angles of attack greater than 2 deg. These data show that the relative heights of the clear ice and horn features is an important factor in considering the aerodynamic effects of SLD accretions. In contrast, the effect of the nodule simulations downstream of the horns were found to have little effect on the aerodynamic performance. Tests with several different nodule simulations produced no measurable performance differences over the baseline simulations with horns present. This indicates that the accurate simulation of the nodule features are not critical in terms of obtaining SLD-ice contaminated airfoil performance estimates.

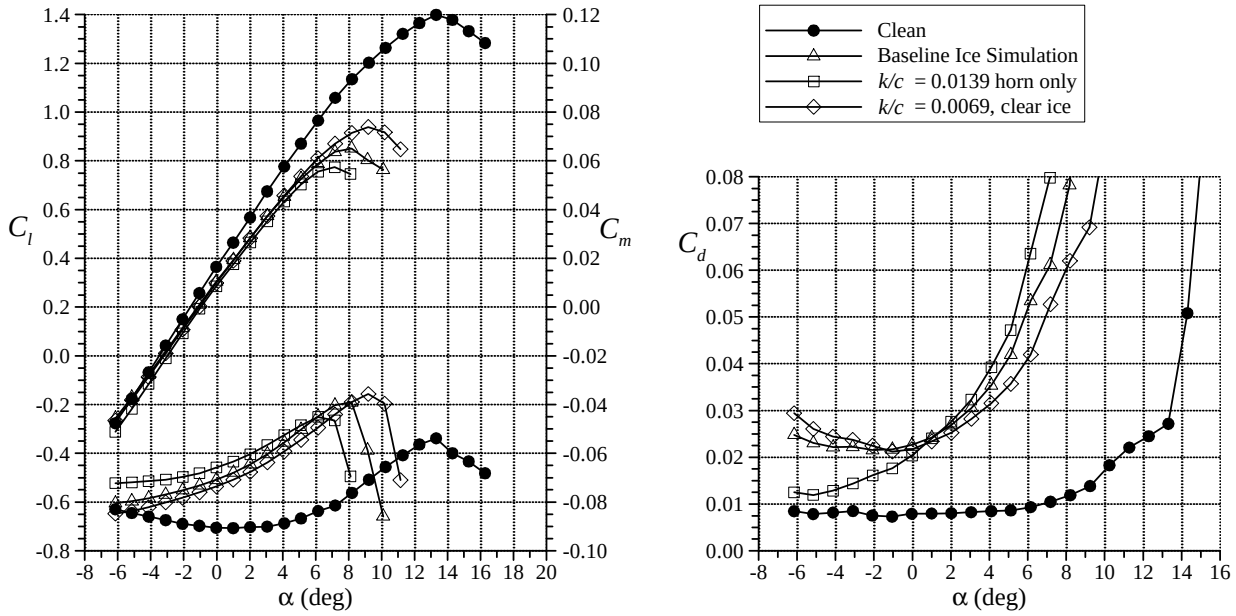

Figure 28. Aerodynamic performance comparison of the baseline SLD ice accretion simulation with the horn-only case and increased clear ice thickness (cf. Table 5).

The importance of the nodule simulations was observed in ice accretion simulation testing of the second category—those shapes without horn features. Table 6 summarizes the baseline ice simulations for the examples of this type. Figure 29 illustrates the effect of combining the clear ice and nodule simulations as well as the effect of the upper surface nodule pattern. First, the maximum lift characteristics show that both the simulated clear ice and nodules contributed to the reduction from the clean configuration. The $C_{l,max}$ values here, in the range of 0.90 to 1.00, were lower than for the airfoil with each of the ice feature simulations tested individually (cf. Figs. 22 and 24). The chordwise locations of the ice feature simulations tested individually was slightly different from the combined simulation. However, this difference was likely not large enough to alter this conclusion. It is not clear in the drag data, why the aligned upper surface nodules resulted in higher values up to α = 5 deg. The lower drag for this configuration (above 5 deg. in Fig. 29), is consistent with the individual nodule simulation results.

The maximum lift characteristics in Fig. 30 further illustrate the effects of the clear ice and nodule simulations. Again, the combined ice accretion simulation resulted in lower $C_{l,max}$ than for the features tested individually. The effect of nodule size and density was also preserved in the combined ice accretion simulation. As indicated in Table 6, the baseline case had three rows of k/c = 0.0057 hemispheres on the upper surface. The first modification in Fig. 30 changed this to 2 rows of k/c = 0.0063 hemispheres, also with 2-D offset spacing. The result was a slight increase in $C_{l,max}$ and C_d for α > 5 deg. These results were consistent with Fig. 20 where only the upper surface nodule patterns were tested. Although the surface location was different in Fig. 20, similar results would be expected at the location in Fig. 30. Figure 30 also illustrates the importance of the relative height of the clear ice simulation to the nodule simulation. In the baseline case, the clear ice simulation had height k/c = 0.0043. In the second modification in Fig. 30, this was increased to 0.0069 which was larger than the k/c = 0.0057 nodules. The results showed an improvement in maximum lift characteristics similar to the ice accretion with horn cases. However, drag was increased for angles of attack less than 6 deg.

The results from aerodynamic testing of SLD ice accretion simulations without horn features indicated that it was important to accurately model both the clear ice and nodule regions. This means that determining the nodule size, spacing and surface extent and clear ice thickness and surface extent are important parameters in determining the proper aerodynamic performance.

Table 6. Baseline Ice Simulations for Figs. 29 and 30.

Lower Surface Nodule Simulation	Lower Surface Horn Simulation	Clear Ice Simulation	Upper Surface Horn Simulation	Upper Surface Nodule Simulation
k/c = 0.0057, from x/c = 0.042 to 0.096 2-D offset spacing	None	From x/c = 0.042 LS to 0.006 US Fig. 29: k/c = 0.0031 Fig. 30: k/c = 0.0043	None	k/c = 0.0057, from x/c = 0.006 to 0.049 2-D offset spacing

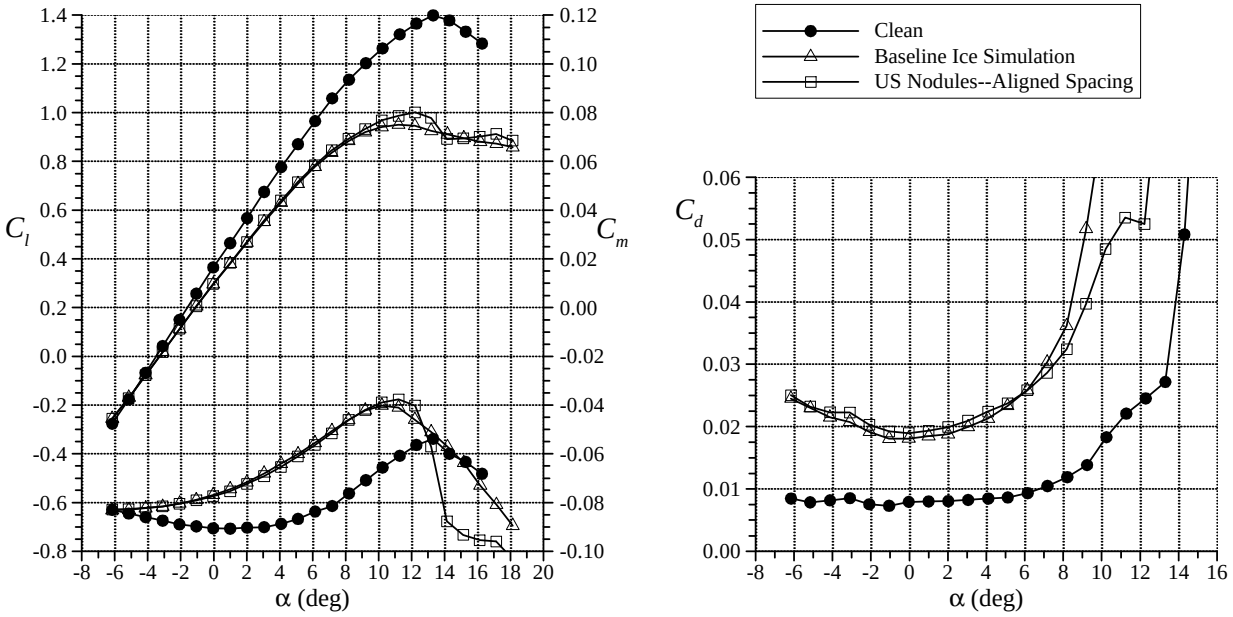

Figure 29. Aerodynamic performance comparison of the baseline SLD ice accretion simulation with a variation in upper surface nodule pattern (cf. Table 6).

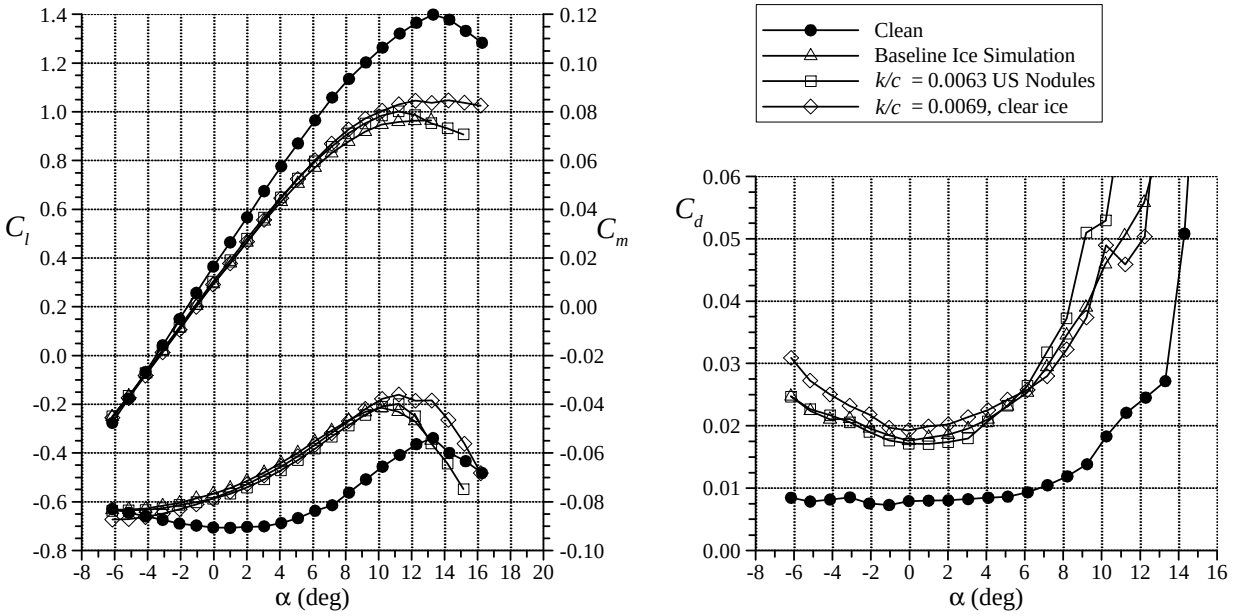

Figure 30. Aerodynamic performance comparison of the baseline SLD ice accretion simulation with a variation in upper surface nodule size and clear ice thickness (cf. Table 6).

IV. Summary and Conclusions

The objectives of this investigation were to identify and document key features of SLD ice accretions on unprotected surfaces and determine their aerodynamic penalties. An icing-tunnel test was carried out using a 77.25-inch chord commuter-class airfoil wing model. Icing runs were performed at airspeeds of 120 and 180 kts and angles of attack of -1 and 3 deg. The SLD cloud conditions had an *MVD* of 133 μm and the *LWC* ranged from 0.32 to 0.55 g/m^3. Three key ice features common to the SLD accretions were identified from these tests: nodules, horns and clear ice. The clear ice region formed in the vicinity of the airfoil stagnation point and had a conformal surface. Horn structures formed downstream of the clear ice region for some cases. The horn structures seemed to form from a coalescence of individual nodules. The nodules formed downstream of the clear ice region, or horns if present, and were similar to large glaze or rime feather-type structures. They had a large variation in size, density, spacing and alignment. These three features were simulated in the follow-on aerodynamic testing. Some icing runs were also performed at scale conditions designed to simulate lower cloud *LWC* than could be obtained in the tunnel. Qualitative comparisons of the resulting ice accretions indicated that the scaling method did produce characteristics that could be associated with lower *LWC*. Further, qualitative comparisons of the ice accretions obtained in the icing tunnel showed good agreement with documented in-flight ice accretions.

The aerodynamic testing was carried out at the University of Illinois using an 18-inch chord model with the same airfoil section as the icing model. The nodules, horns and clear ice features were simulated with simple geometric materials and scaled in size by the ratio of the chord lengths between the icing-tunnel and aerodynamic models (18.0/77.25). The aerodynamic testing was performed at $Re = 1.8\times10^6$ and $Ma = 0.18$. Each of the simulated ice features was tested on the airfoil individually to evaluate their aerodynamic effect. The nodules were simulated with hemispheres, so that the size, spacing and alignment pattern could be closely controlled. Tests with the simulated nodules applied to the airfoil upper surface resulted in maximum lift values of 1.05 to 1.15, reduced from the clean value of 1.40. In general, a larger number of smaller nodules resulted in lower maximum lift and higher drag. Lower maximum lift values were also obtained when the nodules were located closer to the airfoil leading edge. This trend was also observed in tests with the simulated clear ice since this was located at the leading edge and stagnation point. Larger and rougher clear ice simulations resulted in lower maximum lift and higher drag. The maximum lift values for the airfoil with the clear ice simulations was generally in the range of 1.05 to 1.15. The horn simulations had the largest aerodynamic penalties with maximum lift values in the ranges of 0.50 to 0.80. Typical horn effects were observed—larger horns located farther aft resulted in larger degradations. The presence of a lower surface horn resulted in negative stall at very low angle of attack, but had little effect on positive stall when an upper surface horn was also simulated on the airfoil. The lower surface horns also had a large effect on the drag at low angles of attack.

In the second phase of the aerodynamic testing, the individual features were combined to simulate complete SLD accretions. For cases where horns were present, this feature dominated the aerodynamics. The effect of nodules downstream of the horns was very small, if not insignificant. In contrast, the size and chordwise extent of the clear ice region upstream of the horn had a large effect on performance. The performance of the airfoil with the clear ice and horn simulations combined was better (increased maximum lift and decreased drag) than with only the horn simulation present. The relative size of the clear ice and horn features was important in determining the proper aerodynamic performance. For SLD ice accretions without horns, the clear ice and nodule features both affected performance. Trends observed in the testing of the individual features were also observed when the two features were combined. This means that the nodule size, spacing and extent and the clear ice thickness and chordwise extent were important factors in the resulting performance.

Acknowledgements

The authors at the University of Illinois were supported, in part, by FAA grant DTFA MB 96-6-023. The authors wish to thank Jim Riley and Gene Hill of the FAA for supporting this research and for their helpful comments and suggestions. The Icing Branch at NASA Glenn also deserves recognition for supporting the IRT testing component of this study. The IRT crew helped to ensure a productive and successful icing test. Finally, many thanks are due to Gene Addy of NASA Glenn for the contributions of his expertise to this research.

References

[1]Bragg, M.B., "Aircraft Aerodynamic Effects due to Large Droplet Ice Accretions," AIAA Paper 96-0932, 34th Aerospace Sciences Meeting & Exhibit, Reno, NV, Jan. 1996.

[2]Ashenden, R., Lindburg, W., and Marwitz, J., "Two-Dimensional NACA 23012 Airfoil Performance Degradation by Super Cooled Cloud, Drizzle and Rain Drop Icing," AIAA Paper 96-0870, 34th Aerospace Sciences Meeting & Exhibit, Reno, NV, Jan. 1996.

[3]Ashenden, R., Lindburg, W., and Marwitz, J., "Airfoil Performance Degradation by Super Cooled Cloud Drizzle and Rain Drop Icing," *Journal of Aircraft*, Vol. 33, No. 6, Nov.-Dec., 1996, pp. 1040-1046.

[4]Miller, D.R., Addy, H.E., Jr., and Ide, R.F., "A Study of Large-Droplet Ice Accretion in the NASA Lewis IRT at Near-Freezing Conditions," AIAA Paper 96-0934, 34th Aerospace Sciences Meeting & Exhibit, Reno, NV, Jan. 1996.

[5]Addy, H.E. Jr., Miller, D.R., and Ide, R.F., "A Study of Large-Droplet Ice Accretion in the NASA Lewis IRT at Near-Freezing Conditions, Part 2," NASA TM-107424, Apr. 1997, Prepared for the International Conference on Aircraft Inflight Icing, FAA, Springfield, VA., 1996.

[6]Lee, S., and Bragg, M.B., "Experimental Investigation of Simulated Large-Droplet Ice Shapes on Airfoil Aerodynamics," *Journal of Aircraft*, Vol. 36, No. 5, Sept.-Oct., 1999, pp. 844-850.

[7]Addy, H.E. Jr., "Ice Accretions and Icing Effects for Modern Airfoils," NASA TP-2002-210031 also DOT/FAA/AR-99/89, Apr. 2000.

[8]Bond, T.H., Miller, D.R., and Potapczuk, M.G., "Overview of SLD Engineering Tools Development," AIAA Paper 2003-0386, 41st Aerospace Sciences Meeting & Exhibit, Reno, NV, Jan. 2003.

[9]Miller, D.R., Ratvasky, T.P., Bernstein, B.C., McDonough, F., and Strapp, J.W., "NASA/FAA/NCAR Supercooled Large Droplet Icing Flight Research: Summary of Winter 96-97 Flight Operations," AIAA Paper 98-0577, 36th Aerospace Sciences Meeting & Exhibit, Reno, NV, Jan. 1998.

[10]Bernstein, B.C., Ratvasky, T.P., Miller, D.R., and McDonough, F., "Freezing Rain as an In-Flight Icing Hazard," NASA TM-2000-210058, June 2000.

[11]Ide, R.F., and Oldenburg, J.R., "Icing Cloud Calibration of the NASA Glenn Icing Research Tunnel," AIAA Paper 2001-0234, 39th Aerospace Sciences Meeting & Exhibit, Reno, NV, Jan. 2001.

[12]Anderson, D.N., "Manual of Scaling Methods," NASA/CR-2004-21875, Mar. 2004.

[13]Anderson, D.N., and Tsao, J.C., "Evaluation and Validation of the Messinger Freezing Fraction," AIAA Paper 2003-1218, 41st Aerospace Sciences Meeting & Exhibit, Reno, NV, Jan. 2003.

[14]Messinger, B.L., "Equilibrium Temperature of an Unheated Icing Surface as a Function of Airspeed," *Journal of the Aeronautical Sciences*, Vol. 20, No. 1, Jan. 1953, pp. 29-42.

[15]Shin, J., "Characteristics of Surface Roughness Associated with Leading Edge Ice Accretion," AIAA Paper 94-0799, 32nd Aerospace Sciences Meeting & Exhibit, Reno, NV, Jan. 1994.

[16]Cober, S.G., Isaac, G.A., Shah, A.D., and Jeck, R., "Defining Characteristic Cloud Drop Spectra From In-Situ Measurements," AIAA Paper 2003-0561, 41st Aerospace Sciences Meeting & Exhibit, Reno, NV, Jan. 2003.

[17]Potapczuk, M.G., Miller, D.R., Ide, R.F., and Oldenburg, J.R., "Simulation of a Bi-modal Large Droplet Icing Cloud in the NASA Icing Research Tunnel," AIAA Paper 2005-0076, 43rd Aerospace Sciences Meeting & Exhibit, Reno, NV, Jan. 2005.

[18] Lee, S., "Effect of Supercooled Large Droplet Icing on Airfoil Aerodynamics," Ph.D. Dissertation, Dept. of Aeronautical and Astronautical Eng., Univ. of Illinois, Urbana, IL, 2001.

[19]Rae, W.H., and Pope, A., *Low-Speed Wind Tunnel Testing*, Wiley, New York, 1984, pp. 349-362.

[20]Kline, S.J., and McClintock, F.A., "Describing Uncertainties in Single-Sample Experiments," *Mechanical Engineering*, Vol. 75, Jan. 1953, pp. 3-8.

[21]Coleman, H.W., and Steele, W.G., *Experimentation and Uncertainty Analysis for Engineers*, John Wiley and Sons, New York, 1989, pp. 40-118.

[22]Lee, S., and Bragg, M.B., "Experimental Investigation of Simulated Large-Droplet Ice Shapes on Airfoil Aerodynamics," *Journal of Aircraft*, Vol. 36, No. 5, Sept.-Oct. 1999, pp. 844-850.

[23]Broeren, A.P., and Bragg, M.B., "Effect of Airfoil Geometry on Performance with Simulated Intercycle Ice Accretions," AIAA Paper 2003-0728, 41st Aerospace Sciences Meeting & Exhibit, Reno, NV, Jan. 2003.

[24]Lee, S., Ratvasky, T.P, Thacker, M., and Barnhart, B., "Geometry and Reynolds Number Scaling on Iced Business Jet Wing," AIAA Paper 2005-1068, 43rd Aerospace Sciences Meeting & Exhibit, Reno, NV, Jan. 2005.

[25]Brumby, R.E., "Wing Surface Roughness – Cause and Effect," *D.C. Flight Approach*, Jan. 1979, pp. 2-7.

[26]Kim, H.S., and Bragg, M.B., "Effects of Leading-Edge Ice Accretion Geometry on Airfoil Aerodynamics," AIAA Paper 99-3150, June 1999.

[27]Papadakis, M., Alansatan, S., and Seltmann, M., "Experimental Study of Simulated Ice Shapes on a NACA 0011 Airfoil," AIAA Paper 99-0096, Jan. 1999.